UNIVERSITA' POLITECNICA DELLE MARCHE
FACOLTA' DI INGEGNERIA

CORSO DI LAUREA TRIENNALE DI INGEGNERIA INFORMATICA E DELL'AUTOMAZIONE

Manovre di Rendezvous e Riorientamento in Presenza di Detriti Spaziali e Vincoli Direzionali

Rendezvous and Reorientation Maneuvers in the Presence of Space Debris and Directional Constraints

Relatore:
Prof. Simone Fiori

Laureando:
Luca Sabatini

A.A. 2022/2023

1 Abstract

The present work aims to present a list of scripts to model, simulate and control a spacecraft in the presence of obstacles due to its proximity to a space station or other objects orbiting in space. Two maneuvers will be studied in depth along with their modeling and simulation, these will be called respectively reorientation under directional constraints and rendezvous in the presence of physical obstacles. The mathematical model of the roto-translational motion of a spacecraft as well as the design of control fields are entirely written by coordinate-free Lie-group-type formulations. A series of numerical experiments extends the theoretical behavior and illustrates the achievements to present the reader with the most convenient control strategy.

2 Italian Summary

In questa sezione verrà proposto un resoconto in lingua italiana del lavoro esposto in seguito in lingua inglese.

La presente tesi di laurea illustra inizialmente una serie di concetti teorici propedeutici alla comprensione delle scelte compiute nella creazione di algoritmi per la navigazione e il riorientamento di un satellite di piccole dimensioni e senza equipaggio umano. In seguito, sono riportati i risultati delle copiose simulazioni numeriche necessarie al raggiungimento delle versioni finali degli algoritmi proposti.

Nella sezione 3 vengono presentate le motivazioni che hanno spinto l'autore al completamento di questa tesi e l'ambito in cui si intende andare ad operare. Vengono illustrate inoltre le fasi principali della manovra di *Rendezvous*. Quest'ultima consiste nell'eseguire operazioni orbitali pianificate con alta precisione al fine di far incontrare due oggetti spaziali, in questo caso un satellite di piccole dimensioni ed una stazione spaziale (per esempio la ISS 1). L'operazione di *Rendezvous* può essere divisa rispettivamente in cruising-phase e docking-phase, la prima si riferisce allo spostamento del satellite da un predeterminato punto iniziale (in genere non nella stessa orbita della stazione spaziale) fino alle prossimità della ISS, mentre la seconda inizia da una dozzina di metri dal docking port 2 e si conclude con il corretto agganciamento del satellite alla stazione spaziale. Data la copiosa quantità di detriti spaziali di tipo artificiale (porzioni di altri satelliti) o naturale (rocce spaziali) sorge la necessità di equipaggiare i computer di bordo dei satelliti con un sistema di *Obstacle Avoidance* in grado di evitare danni da impatto con gli oggetti appena menzionati grazie alle informazioni fornite dai sensori di cui il satellite si suppone sia equipaggiato.

La natura dei satelliti menzionati è di solito riconducibile allo studio dell'ambiente spaziale che li circonda, per esempio la digitalizzazione di immagini di galassie lontane o stelle. Solitamente questi dispongono di strumentazione come telescopi, sensibili però, alle fonti luminose come il sole o la luna che li possono rovinare ed eventualmente rendere fuori uso. Per questo motivo è stato implementato un secondo algoritmo volto alla riorientazione del satellite e tenendo in considerazione vincoli direzionali dettati dalla direzione degli oggetti luminosi. Inoltre, essendo satelliti autonomi, sorge la necessità di mantenere l'antenna principale del satellite sempre diretta verso la terra per ricevere eventuali istruzioni o semplicemente per monitorare il suo comportamento dalla stazione di terra. Dunque oltre ad evitare fonti eccessivamente luminose, l'algoritmo creato è anche in grado di mantenere sempre l'asse con guadagno massimo dell'antenna in una direzione tale da permettere lo scambio di dati con la base e contemporaneamente portare a termine la missione cioè puntare un ipotetico telescopio da una direzione iniziale a quella successiva senza deteriorare la strumentazione a bordo.

Contents

List of Figures

List of Tables

3 Introduction

Autonomous guidance of small-sized unmanned spacecrafts has been a goal in applied research since the inception of space missions. Autonomous guidance is able to overcome communications delays with the ground mission guidance station while benefiting from direct on-site obstacle sensing and avoidance. Current and future orbital missions involve operations in the proximity of large space structures[27], such as the International Space Station. Rendezvous operations constitute a

Figure 1: A view of the International Space Station (ISS) reproduced from en.wikimedia.org.

vital step in unmanned spacecrafts missions to extend their operational life, as it allows on-orbit refueling of cold gas propellants and maintenance [4]. Rendezvous may be broken down into a *cruising phase*, during which the spacecraft leaves its orbit to approach the space station, and a *docking phase*, which starts a few dozens of meters away from the station and lead the spacecraft to physically conjoin the space station through one of the available docking ports shown in Figure 2.

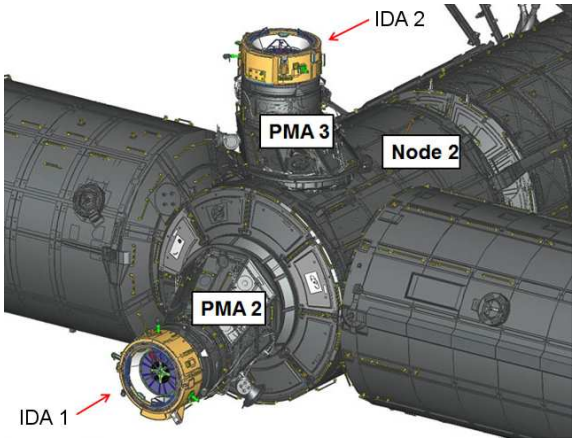

Figure 2: Example of an ISS module designed for docking, PMA stands for Pressurized Mating Adapter while IDA stands for International Docking Adapter. Source:en.wikimedia.org

While the docking phase concerns precision guidance and collision avoidance with the space station, guidance along the cruising phase is heavily affected by physical obstacles which may be moving or fixed with respect to the station and the spacecraft. Obstacles may be active satellites, micrometeoroids or space debris, parts of vehicles arisen from collisions still in orbit around the Earth. A serious accident on records happened in February 2009, when Iridium-33 communication satellite and Kosmos-2251 (non-operating) military satellite accidentally collided [5] at an altitude of 776 km above the territory of Siberia at a speed of 11.7 km/s. Both satellites were destroyed in the impact producing more than 2,300 fragments. One third of such fragments entered the

Figure 3: Logo of the Orbital Debris Program Office (ODPO) reproduced from orbitaldebris.jsc.nasa.gov.

atmosphere and disintegrated, while the rest is still orbiting the Earth today. A large number of space debris orbiting the Earth are currently being watched upon by NASA through the Orbital Debris Program Office whose logo is reproduced in Figure 3. Reorientation of a spacecraft is likewise a fundamental operation to be carried out during an exploratory mission. Large-angle attitude slew maneuvers are required to achieve retargeting of payload instrumentation during science missions [28]. Reorientation from one direction to another must be operated in such a way that the boresight[1] of sensitive instrumentation, such as cryogenically cooled infrared telescopes [28] and star sensors [17], is not directed toward any bright object such as the sun, the Earth or the moon, while the antenna does not loose communication with the ground or the space station [16]. In particular, boresight evasion introduces the notion of attitude forbidden constraints [17]. Automated reorientation in the presence of attitude constraints poses a challenging computational task for the on-board guidance control system [24].

Automated reorientation plays a crucial role even during the docking phase since safe docking may take place only if the docking axis of the spacecraft is precisely oriented along the docking axis of the station docking port. In this phase, orientation is supposed to happen with extreme precision, facilitated by the alleged absence of directional obstructions.

The mathematical representation to model the roto-translational dynamics of a spacecraft, as well as the control strategy to make a spacecraft execute the necessary movements in space, are a subject of continued debate in the scientific community. In particular, the mathematical representation of the rotational dynamics may be picked from the realms of Tait-Bryan representation, quaternions and rotation matrices.

Tait-Bryan angles carry an intuitive and easy-to-visualize value [34], although the conversion from angular to Cartesian coordinate is burdened by complex trigonometric expressions and from inherent singularities [24]. Quaternion-based representations are often invoked in aerospace engineering [24], although quaternions are affected by the well-known problem of unwinding due to the redundancy of the unit quaternion (namely, when the rotation angle is sufficiently large, the trajectory of attitude maneuver may be longer, leading to increased propellant consumption and longer maneuver time) [17]. In addition, in the author's opinion, quaternion machinery results in unnecessarily complicated expressions that directly affect modeling as well control design. Although inherently redundant, coordinate-free rotation-matrices representations result to be singularity free [7] and easy to manage in modeling and control design thanks to the underlying theory of Lie groups [9, 13, 14], hence rotation-matrices representations are the mathematical tool of choice in the present research endeavor.

Automated control of rigid bodies, such as drones, satellites, ground robots as well as remotely

[1]Boresight: The term boresight came from high-gain antennas such as parabolic dishes, which produce narrow, pencil-shaped beams. In this case the term will be referred to the main axis the instruments onboard.

operated underwater vehicles, may benefit from the theory of virtual attractive-repulsive potentials, which has been explored and extended across the decades [2, 18, 19, 20, 22, 23, 25, 26, 31, 33, 36]. Artificial-potential-based control relies on artificial potential functions constructed so as to assign a potential value to each point of the state space in a way that promotes state transition toward a set goal while demoting state transitions toward undesired obstructions. In particular, it is important to cite the papers: [29] that revise and utilizes gradient-based control fields in conjunction with further physically-plausible forces, [12] that extended the theory of virtual attractive-repulsive potential to control the rotational dynamics by Lie-group theory, and the paper [24] that introduced the notion of barrier-type potentials to control the attitudinal dynamics of a spacecraft (in quaternion representation).

The aim of this thesis is to devise a complete navigation and attitude control strategy for a spacecraft bound to an orbital station to effect space missions and automated docking. After recalling the principal equations governing the motion of an orbital spacecraft, it will be presented a control strategy to effect reorientation under mandatory/forbidden directional constraints. In addition, a multiobjective control strategy will be presented to make a spacecraft approach safely an orbital station while avoiding still or moving obstacles, until the final guidance phase that guarantees collision-free docking with the correct attitude.

A distinguishing feature of this work endeavor is that attitudes are represented through orthogonal rotation matrices and that the corresponding control actions are represented through vector fields on the space of skew-symmetric matrices. These matrices are treated as a whole, without any need to resort to angles nor scalar velocities. Although as a matter of fact it is difficult for engineers to free themselves from the need to make use of scalar variables, the present paper, among other, shows that it is in fact convenient. A relation between quaternion and rotation-matrix representations is discussed in the Appendix.

3.1 Organization of contents

The content is organized as follows in the present thesis, Section 4 recalls necessary details from orbital dynamics, including the set of reference frames used to describe the equations of motion and the kinds of propulsion systems available within a small-sized spacecraft. Section 5 details the notion of spacecraft reorientation under directional constraints, with special emphasis on mandatory and forbidden cones of the celestial sphere. In this section, appropriate virtual attractive-repulsive potentials to achieve reorientation are presented along with related gradient-type control torque terms. Section 5.4 of this document discuss rendezvous of the spacecraft with the main station by breaking down a rendezvous maneuver task into three subtasks, namely: cruising in the presence of (possibly moving) obstacles, far-end and near-end docking. Each subtask is discussed and tackled separately through an appropriate control strategy adapted to the required degree of precision needed. The general control strategy follows a speed control paradigm, based on sliding mode control, aided by virtual attractive-repulsive potential theory. Section 6 illustrates the theoretical content of this project through an extensive series of numerical experiments based on several cases-of-study from the scientific literature. Section 7 concludes the document and suggests a number of possible improvements to the current endeavor to be tackled in future research projects.

4 Reference frames, physical model and equations of motion

The present section aims at recalling a number of essential details concerning the reference frames used to describe the equations of motion of a small-sized spacecraft, the type of physical actuators that govern such motion and a mathematical model of motion. Within this section, the terminology that shall be used within this document will be recalled as well.

4.1 Spacecraft features

The scenario taken into consideration in the present work involves a main *station*, which is assumed to stay in a stable orbit[2] around the Earth and to be controlled directly by a ground station or by on-board personnel and is hence operated independently. The scenario also involves a small-sized unmanned *spacecraft*, endowed with a sensor (e.g., a telescope) to achieve scientific missions as well as a communication device (e.g., a radio antenna) to keep in touch with the ground station and/or the main station, and an on-board autonomous control system that is able to provide appropriate navigation and control actions relative to objects around it.

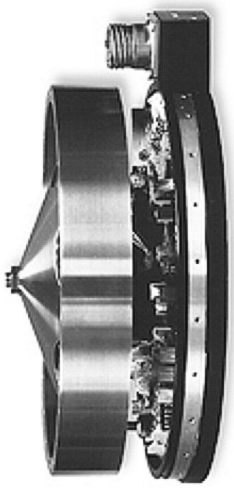

Figure 4: A sideview of a small reaction wheel used to modify a spacecrtaft's attitude from en.wikipedia.org.

In the examined scenario, the small spacecraft, whose control is the main subject of present investigation, is supposed to be endowed with two series of actuators, namely a series of cold-gas-based *reaction thrusters* that serve to control its translational dynamics, and a series of *reaction wheels* depicted in figure number 4 that serve to control its rotational dynamics [4]. We shall assume that the number and disposition of thrusters and wheels are appropriate to make the spacecraft fully operated to ensure that the control actions generated by the devised control algorithm find appropriate realization.

To what concerns the cold gas ejecting thrusters, it is assumed that their thrust cannot be modulated and is either null (when 'off') or maximum (while 'on'). Conversely, the spacecraft is assumed to be endowed with three reaction wheels (one per axis) through which it is possible to modulate any sort of active torque. (Special instances of under-actuated systems are studied, e.g., in [3].) A view of a small spacecraft is reproduced in Figure 5.

[2] A stable orbit is considered having a trajectory that completes perfect circles around earth (Geocentric) this happens when the height of the orbit is relatively small

Figure 5: A pictorial view of a small-sized spacecraft reproduced from https://www.nasa.gov.

4.2 Reference Frames

4.2.1 Inertial Reference Frame

An *inertial* reference frame $\mathcal{F}_\mathrm{I}$ is introduced to describe the direction of bright objects whose direct light exposure should be avoided, such as the sun, the Earth, the moon. The inertial reference frame $\mathcal{F}_\mathrm{I}$ is also necessary to specify the direction of a celestial object to be observed by pointing a telescope to it. Finally this reference frame is used to match the boresight of a transmitting antenna located on a ground station. Such reference frame is introduced on the condition that the mentioned directions stay constant within the timespan of a given mission. Target attitudes, mandatory and forbidden pointing directions during reorientation maneuvers are referred to the frame $\mathcal{F}_\mathrm{I}$.

4.2.2 Fixed Reference Frames

There are two Fixed Reference Frames that will be introduced.

Firstly a *station-fixed* reference frame $\mathcal{F}_\mathrm{S}$. Such reference frame is concordant with the space station and plays a fundamental role during rendezvous maneuvers and docking because in this phase the spacecraft takes as docking reference the main axis of the port, expressed using this Fixed Frame. In addition, during the cruising phase of rendezvous maneuver, the dynamics of the spacecraft is expressed in terms of the location of the station through the Clohessy-Wiltshire equations, which are valid for objects orbiting the Earth on circular orbits and that are spaced apart of a few kilometers. The station-fixed reference frame $\mathcal{F}_\mathrm{S}$ is sometimes referred to as 'local vertical, local horizontal' (LVLH) see Fig 6. Among the three orthogonal axes, one is directed from the center of the station to the center of the Earth (R_bar or Z_LVLH) and is associated a unit-vector $e_\mathrm{z} := [0\ 0\ 1]^\top$, one is directed tangentially to the orbit in the direction of motion (V_bar or X_LVLH) and is associated a unit-vector $e_\mathrm{x} := [1\ 0\ 0]^\top$. The third axis (labeled either H_bar or Y_LVLH) is oriented so as to form a right-handed frame with the former two. The symbol $^\top$ denotes matrix transpose.

A spacecraft-fixed reference frame $\mathcal{F}_\mathrm{C}$ is introduced as well, which serves to describe the relative orientation and location of the spacecraft with respect to the inertial frame $\mathcal{F}_\mathrm{I}$ or the station-fixed frame $\mathcal{F}_\mathrm{S}$, depending on the maneuver being effected. (The subscript C stems from the fact that, in the rendezvous literature, the spacecraft is often referred to as *chaser*.) The Cartesian axes of the reference frame $\mathcal{F}_\mathrm{C}$ are assumed to be aligned to the principal axes of inertia of the spacecraft. The relative orientation and location enters the control goals to be fulfilled by the spacecraft.

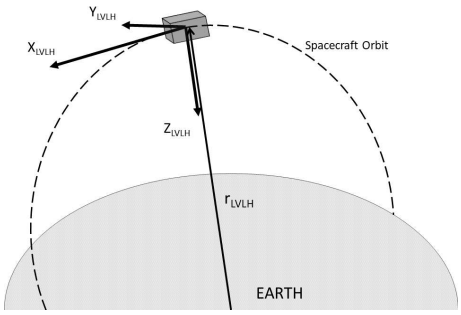

Figure 6: A pictorial view of the LVLH reference frame relative to an orbiting spacecraft reproduced from [4]

4.3 Physical model and equations of motion

Under the assumption that the station and the spacecraft are both orbiting the Earth at slightly different quotas, the translational motion of the spacecraft in the station-fixed reference frame $\mathcal{F}_{\mathrm{S}}$ may be described through the Clohessy-Wiltshire equations. The Clohessy–Wiltshire equations describe a simplified model of orbital relative motion, in which both the station and the spacecraft are in a circular orbit. The Clohessy–Wiltshire model provides a first-order approximation of the spacecraft's motion in a station-fixed reference frame [8].

Denoting by p the coordinate vector of the spacecraft with respect to the station-fixed reference frame $\mathcal{F}_{\mathrm{S}}$, the Clohessy–Wiltshire model reads

$$m\ddot{p} = f_{\mathrm{rt}} + f_{\mathrm{cc}} + f_{\mathrm{vd}} + f_{\mathrm{rd}},\ p(0) = p_0,\ \dot{p}(0) = v_0, \tag{1}$$

where the term f_{rt} denotes the resultant of the mechanical forces exerted by the reaction thrusters on the body of the spacecraft, f_{vd} denotes viscous drag due to friction with atmospheric particles, the term f_{cc} denotes the resultant of fictitious forces (Coriolis and centrifugal), f_{rd} denotes the resultant of random disturbances affecting the motion of the spacecraft and m denotes the total mass of the spacecraft at a given time.

The fictitious force term takes the expression

$$f_{\mathrm{cc}} := m \begin{bmatrix} 0 & 0 & 0 \\ 0 & -\omega_0 & 0 \\ 0 & 0 & 3\omega_0^2 \end{bmatrix} p + m \begin{bmatrix} 0 & 0 & -2\omega_0 \\ 0 & 0 & 0 \\ -2\omega_0 & 0 & 0 \end{bmatrix} \dot{p}, \tag{2}$$

where ω_0 denotes the orbital rate of the main station. For a circular orbit around a central body, the orbital rate is assumed to be constant and is evaluated through the expression $\omega_0 = \sqrt{\mu/r^3}$, where r denotes the radius of the circular orbit traveled by the station and μ denotes a standard gravitational parameter [32]. (In the present context, the standard gravitational parameter reads $\mu = GM$, where G denotes the universal gravitational constant and M denotes the Earth's mass.)

The viscous drag is considered to be non-negligible only in the direction of motion (corresponding to the axis $\mathrm{V}_{\mathrm{bar}}$ of the LVLH system), hence the braking force takes the expression

$$f_{\mathrm{vd}} := -\tfrac{1}{2}\rho V_0^2 S C_{\mathrm{D}} e_{\mathrm{x}}. \tag{3}$$

where ρ denotes the density of the atmosphere, V_0 denotes the orbital speed of the spacecraft, S denotes the frontal cross-section area of the spacecraft and C_{D} denotes a drag coefficient. The orbital speed may be written in terms of the orbital rate as $V_0 = r\,\omega_0$ and is henceforth constant. All the others known perturbations can be considered orders of magnitude smaller than the drag force and so negligible. Further forcing terms, essentially of random nature, are taken into account through the disturbance force f_{rd}.

To what concerns the rotational dynamics, the spacecraft is considered as a rigid body acted upon by a series of mechanical torques due to the reaction wheels and external disturbances.

A constructive detail to bear in mind regarding the transational dynamics of the spacecraft is that the thrusters are arranged in such a way (in [4] a section shows the distribution of the thrusters) that two of them are eventually switched on at once in order to exert a null torque on the spacecraft body. Such design aids control development since it essentially decouples translational-oriented actuation from rotational-oriented actuation.

The attitude of a spacecraft with respect to the space station is quantified by a rotation matrix $R \in \mathrm{SO}(3)$ (namely, a special orthogonal matrix). Such rotation matrix is defined to be the one that aligns the spacecraft-fixed reference frame $\mathcal{F}_{\mathrm{C}}$ to either the inertial reference frame $\mathcal{F}_{\mathrm{I}}$ or to the station-fixed reference frame $\mathcal{F}_{\mathrm{S}}$, depending on what is the current maneuver being described. The equations of motion may be derived in a standard minimal-action variational setting which leads to classical Euler-Poincaré equations. Since the spacecraft is subjected to non-conservative torques, such equations are not 'pure' [35].

The rotational dynamics of a rigid body is expressed by a system of two first-order differential equations [9]:

$$\begin{cases} \dot{R} = R\Omega, \ R(0) = R_0, \\ \mathbb{J}\dot{\Omega} = \mathbb{Q}\Omega + T_{\mathrm{rw}} + T_{\mathrm{rd}}, \ \Omega(0) = \Omega_0, \end{cases} \tag{4}$$

where $\dot{R} \in T_R\mathrm{SO}(3)$ denotes the rotational speed-matrix of the spacecraft, $\Omega \in \mathfrak{so}(3)$ denotes the skew-symmetric angular speed-matrix of the spacecraft, the symbol $\mathbb{J} : \mathfrak{so}(3) \to \mathfrak{so}(3)$ denotes the inertia operator, the operator $\mathbb{Q} : \mathfrak{so}(3) \to \mathfrak{so}(3)$ denotes the resultant of inherent torques due to inertia and mass unbalance within the spacecraft, $T_{\mathrm{rw}} \in \mathfrak{so}(3)$ denotes the mechanical torque exerted by the reaction wheels and $T_{\mathrm{rd}} \in \mathfrak{so}(3)$ denotes a random disturbance term. The operator $\mathbb{J}$, which is not a matrix, and the operator $\mathbb{Q}$ stem from the Euler-Poincaré equations of motion on the Lie group SO(3). It is assumed here that the inertia tensor of the spacecraft is constant. The function $\mathbb{J}\Omega$ is hence linear (and invertible) in Ω, while the function $\mathbb{Q}\Omega$ is quadratic.

As it will be clarified in Section 5, it is not necessary to specify the structure of the operator $\mathbb{Q}$, since a fully-actuated system may be controlled under the principle of dynamics replacement [12], based on inherent dynamics deletion. In the model (4), the second equation establishes the rotational speed in the reference frame $\mathcal{F}_{\mathrm{C}}$. The mechanical torque field T_{rw} will depend on the actual attitude R through the chosen control law. The first equation in the system (4), often referred to as 'reconstruction equation', allows one to reconstruct the actual attitude of the spacecraft in the chosen reference frame.

Note that, in the present thesis, the rotation matrix R is the only quantity that is introduced to represent the attitude of a spacecraft, hence quaternions will not be introduced nor Euler nor Tait-Bryan angles. In addition, the matrix R will always be treated as whole, without any needs to resort to its entries or angular coordinates.

The mass of a spacecraft changes over time due to propellant consumption during rendezvous. Since the total mass m enters the equations of dynamics (1), mass decay needs to be taken into account. Mass decay is described through the differential equation [38]:

$$\dot{m} = -\frac{n\bar{f}_{\mathrm{rt}}}{gI_{\mathrm{sp}}}, \ m(0) = m_0. \tag{5}$$

In the above expression, the constant scalar $\bar{f}_{\mathrm{rt}} > 0$ denotes the maximum thrust of each propulsor when 'on', the symbol g denotes the gravitational acceleration, the constant I_{sp} denotes the specific impulse of each propulsor. (Specific impulse is a measure of how efficiently a reaction mass engine creates thrust.) The variable n denotes the number of active thrusters at a given time and may take only the values 0, 2, 4, 6. Mass distribution also affects the rotational inertia of a spacecraft. We shall however assume that the contribution of the propellant mass to the total inertia is negligible, hence the inertia tensor will be considered constant throughout this document.

4.4 Numerical implementation of the equations of motion

All in one, the system (4) constitute a system of differential equations on the tangent bundle $T\mathrm{SO}(3)$, while the the Clohessy–Wiltshire model is a system of differential equations in $\mathbb{R}^3$.

The Clohessy–Wiltshire model may be implemented numerically by the help of a forward Euler numerical scheme. Let us denote the discrete-time counterparts of the position vector as p_s, of the linear velocity $v := \dot{p}$ as v_s, of the resultant of all forces $f := f_{\mathrm{rt}} + f_{\mathrm{cc}} + f_{\mathrm{vd}} + f_{\mathrm{rd}}$ as f_s, and of the mass as m_s, where s denotes the step counter. Denoting by h the numerical time-step, the numerical scheme then reads

$$\begin{cases} v_{s+1} = v_s + h f_s / m_s, \\ p_{s+1} = p_s + h\, v_s. \end{cases} \tag{6}$$

The result of such iteration is a numerical approximation of the actual trajectory, namely the quantity p_s is an approximation of the actual coordinate vector $p(hs)$. It is worth noting that, in an ideal setting, the orbital translational motion happen on the $x - z$ plane, hence the coordinate y does not play any role in the model.

In a similar way, upon denoting by n_s the discrete-time counterparts of the number of active thrusters, the equation (5) may be solved numerically as

$$m_{s+1} = m_s - \frac{n_s h \bar{f}_{\mathrm{rt}}}{g I_{\mathrm{sp}}}. \tag{7}$$

To what concerns the numerical integration of the equations (4), it pays to introduce discrete-time counterparts of the involved variables, namely R_s for the attitude matrix, Ω_s for the angular speed matrix, and T_s for the resultant torque matrix $T := T_{\mathrm{rw}} + T_{\mathrm{rd}}$. Then the rotational model (4) may be simulated numerically by the following iteration

$$\begin{cases} R_{s+1} = R_s \mathrm{Exp}(h\, \Omega_s), \\ \Omega_{s+1} = \Omega_s + h\, \mathbb{J}^{-1}(\mathbb{Q}\Omega_s + T_s). \end{cases} \tag{8}$$

We shall notice briefly that the first iteration rule stems from the theory of numerical integration of differential equations on Lie-group bundles. In the above relations, the symbol Exp denotes matrix exponential. Interested readers might find more details in the papers [9, 12].

5 Reorientation under directional constraints

The first control problem to be treated is reorientation in the presence of directional constraint. Reorientation consists in generating a control action that changes the attitude of the spacecraft from an initial attitude, represented by a rotation matrix $R_{\mathrm{i}} \in \mathrm{SO}(3)$, to a desired attitude, represented by a rotation matrix $R_{\mathrm{d}} \in \mathrm{SO}(3)$. Without any further constraints, the problem would be solved by the *geodesic* motion (namely, the shortest path in the space $\mathrm{SO}(3)$) from R_{i} to R_{d}. In actual space missions, however, reorientation must take into account directional constraints, which may be classified as

- *mandatory directions*, specified by unit vectors $e_{\mathrm{M},i} \in \mathbb{R}^3$ and angular amplitudes $\theta_{\mathrm{M},i}$, that represent cones of amplitude $\theta_{\mathrm{M},i}$ around given directions $e_{\mathrm{M},i} \in \mathbb{R}^3$, that one of the axis of the spacecraft must always lie within, and
- *forbidden directions*, specified by unit vectors $e_{\mathrm{F},i} \in \mathbb{R}^3$ and angular amplitudes $\theta_{\mathrm{F},i}$, that represent cones of amplitude $\theta_{\mathrm{F},i}$ around given directions $e_{\mathrm{F},i} \in \mathbb{R}^3$, that one of the axis of the spacecraft must always keep out from.

An example of mandatory-type constraint arises from the requirement that the boresight of the main antenna on the spacecraft keeps within the cone of contact of a ground-station antenna. The angles $\theta_{\mathrm{M},i}$ are generally wider than the angles $\theta_{\mathrm{F},j}$, favoring a broader range of motion since the chaser's antenna always has to be inside this area. An example of forbidden-type constraint arises from the necessity to make the boresight of a light-sensitive telescope avoid sunbeams and other brights sources.

An Example of these two types of cones is depicted in figure 7 as a 3D figure, here the satellite is represented as a cube from which the cones extend outwards. The figure is for clarification purposes only but it's important to notice that the mandatory cone is generally broader. Let one of the axes be the one on which the main antenna lies, through the image it is possible to perceive by intuition, how the cube can rotate but only maintaining the ax mentioned inside the green cone, and a similar explanation follows for the forbidden cone. These two behaviors have to be respected at all times during the maneuver described to complete it safely and to ensure that no instruments get damaged.

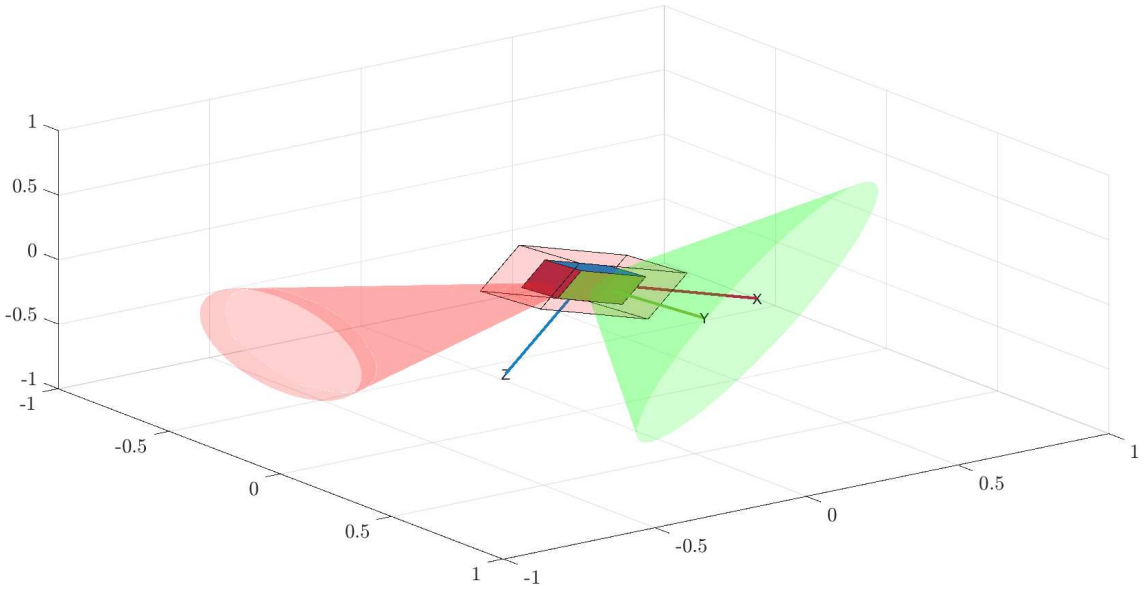

Figure 7: A visual representation of two cones, the red one represent the forbidden direction while the green one represent the mandatory direction both having specific apertures given by precise angles to represent the zones to keep boresight within or out of. This picture was made with the help of MATLAB© by the author.

The directions $e_{\mathrm{M},i}$ and $e_{\mathrm{F},i}$ are generally specified in the inertial reference frame $\mathcal{F}_{\mathrm{I}}$, while the boresight axes of the antenna, hereafter denoted as e_{BA}, and of the sensor, hereafter denoted as e_{BS}, aboard the spacecraft are specified in the spacecraft-fixed reference frame $\mathcal{F}_{\mathrm{C}}$.

Reorientation is effected via virtual potential functions based on the above information. The virtual potential functions defined in the following is based on both an attractive term and on barrier-type repulsive terms and enter the equations of dynamics through their Riemannian gradient.

5.1 Rotational dynamics control by dynamics replacement and a virtual-attractive-repulsive potential

The aim of control design for reorientation purpose is to determine an appropriate control action that affects the rotational dynamics of the spacecraft through equations (4).

In the present research project, the reaction-wheel torque-type control field is taken as

$$T_{\mathrm{rw}} := -\,\mathbb{Q}\Omega - K_{\mathrm{f}}\,\Omega - R^{\top}\nabla_R V, \tag{9}$$

where $V : \mathrm{SO}(3) \to \mathbb{R}$ denotes a virtual attractive-repulsive potential and ∇_R denotes the Riemannian gradient at $R \in \mathrm{SO}(3)$ corresponding to the canonical inner product in the tangent bundle $T\mathrm{SO}(3)$.

The first term on the right-hand side of the relation (9) stems from the principle of dynamics replacement. The purpose of such form of cancellation is to overrule the internal dynamics of a rigid body with the aim of replacing it with a desired dynamics. Such principle may also be referred to as *decoupling* [21].

The second term introduces a sort of rotational braking effect, whose purpose is to slow down the rotational motion and make the effective control torque less sensitive to excessive control actions. This term, discussed in [12, 17, 29], also prevents the control algorithm to oscillate excessively around the optimal solution, which is a well-known effect in gradient-based optimization. The constant $K_{\mathrm{f}} > 0$ determines the relative importance of such term. In general, dissipative forces proportional to speed are added to promote asymptotic stabilization of a dynamical system [21].

The third term on the right-hand side of the relation (9) provides a torque that drives the attitude of the rigid body toward the minimum of the potential function V. The potential function must be cautiously crafted in such a way to effectively drive the spacecraft from the initial attitude to the desired attitude while avoiding undesired (forbidden) direction and yet meeting favorable (mandatory) inclination. Notice that the potential is defined in the inertial reference frame $\mathcal{F}_{\mathrm{I}}$, and so is its Riemannian gradient $\nabla_R V$, hence it needs to be brought back to the spacecraft-fixed reference frame $\mathcal{F}_{\mathrm{C}}$ before entering the equations by a pre-multiplication by the $\mathcal{F}_{\mathrm{I}}$-to-$\mathcal{F}_{\mathrm{C}}$ reference conversion matrix $R^{\top}$.

On the basis of the chosen control law (9), the angular acceleration of the spacecraft reads

$$\mathbb{J}^{-1}(\mathbb{Q}\Omega + T) = \mathbb{J}^{-1}(-K_{\mathrm{f}}\,\Omega - R^{\top}\nabla_R V + T_{\mathrm{rd}}), \tag{10}$$

hence it does not depend on the internal dynamics anymore. According to literature, the inertia matrix of a spacecraft may be taken diagonal (by an appropriate choice of coordinate system $\mathcal{F}_{\mathrm{C}}$) and even isotropic [4, 24]. For the sake of simplification, we shall assume that the three eigenvalue of such matrix take the same value $J_{\mathrm{C}} > 0$, which readily implies that $\mathbb{J}\Omega = J_{\mathrm{C}}\Omega$.

5.2 Additive potential function and related gradient

As a first attempt to define a potential function, based on additive-repulsive potential theory developed in [12, 24, 27], the expression:

$$V_{\mathrm{ADD}}(R) := A(R) + \sum_i B_i(R), \tag{11}$$

is taken, where $A : \mathrm{SO}(3) \to \mathbb{R}$ denotes an attractive potential, whose purpose is to attract the attitude of the spacecraft toward the desired attitude R_{d}, while each $B_i : \mathrm{SO}(3) \to \mathbb{R}$ is a barrier-type repulsive potential aimed at making the spacecraft avoiding the forbidden direction while keeping up with the mandatory directions.

In order to specify the structure of the attractive term, it is necessary to recall the notion of geodesic distance in SO(3). Given two attitudes $R_1, R_2 \in \mathrm{SO}(3)$, their geodesic distance is defined as

$$d(R_1, R_2) := \|\mathrm{Log}(R_1^\top R_2)\|_{\mathrm{F}}, \tag{12}$$

where Log denotes the principal matrix logarithm and the symbol $\|\cdot\|_{\mathrm{F}}$ denotes a Frobenius matrix norm.

Now, the attractive potential is defined as a upside-down bell-shaped function of the geodesic distance between the current attitude and the desired attitude as

$$A(R) := -\tfrac{1}{2} K_{\mathrm{A}} \ell^2 \exp\left(-\frac{d^2(R_{\mathrm{d}}, R)}{\ell^2}\right), \tag{13}$$

which appears to be a monotonically increasing function with a minimum in $R = R_{\mathrm{d}}$. The constant $K_{\mathrm{A}} > 0$ determines the absolute strength of this component of the torque, while the constant $\ell > 0$ represents the radius of influence of the potential over the space SO(3): the larger ℓ, the larger its influence area.

In order to compute the Riemannian gradient of the attractive potential component, it is worth recalling the golden formula (for a review of manifold calculus in system theory and control, interested readers might consult [10, 11]):

$$\nabla_R d^2(R_{\mathrm{d}}, R) = 2R\mathrm{Log}(R_{\mathrm{d}}^\top R). \tag{14}$$

As result the torque term corresponding to the attractive potential is:

$$-R^\top \nabla_R A = -K_{\mathrm{A}} \exp\left(-\frac{d^2(R_{\mathrm{d}}, R)}{\ell^2}\right) \mathrm{Log}(R_{\mathrm{d}}^\top R). \tag{15}$$

The repulsive component of the potential is designed to be of barrier type. In the present endeavor, barriers are designed to either keep a given axis of the spacecraft away from forbidden directions or in the angular proximity of mandatory direction. Let us examine forbidden-cones and mandatory-cones in details.

Given a mandatory direction $e_{\mathrm{M}} \in \mathbb{R}^3$ expressed in the reference system $\mathcal{F}_{\mathrm{I}}$ and an axis of the spacecraft $e_{\mathrm{BA}} \in \mathbb{R}^3$ expressed in the reference system $\mathcal{F}_{\mathrm{C}}$, the cosine of the angle between these two directions is given by $e_{\mathrm{M}}^\top R\, e_{\mathrm{BA}}$, where R denotes the current attitude of the spacecraft with respect to the inertial reference system. In order to make sure that the axis e_{BA} keeps at an angular distance from the mandatory direction e_{M} lesser than a prescribed threshold θ_{M}, the following constraint needs to be imposed

$$e_{\mathrm{M}}^\top R\, e_{\mathrm{BA}} - \cos\theta_{\mathrm{M}} > 0. \tag{16}$$

Such constraint appears as a *linear inequality* in the attitude matrix R.

A barrier potential to secure adherence to such directional constraint reads

$$B_{\mathrm{M}}(R) := -K_{\mathrm{M}} \log(e_{\mathrm{M}}^\top R\, e_{\mathrm{BA}} - \cos\theta_{\mathrm{M}}), \tag{17}$$

where $K_{\mathrm{M}} > 0$ determines the strength of the corresponding torque term in the control action, while log denotes natural logarithm. It is immediate to recognize that, as the axis $R\, e_{\mathrm{BA}}$ gets

closer to the surface of the mandatory cone, hence the difference $e_{\mathrm{M}}^{\top} R\, e_{\mathrm{BA}} - \cos\theta_{\mathrm{M}}$ approaches 0, the function $B_{\mathrm{M}}(R)$ approaches $+\infty$ hence providing an infinitely steep potential wall (a barrier, in fact).

The above barrier-type virtual potential component is designed to produce an artificial repulsion from the surface of an obstacle, which is represented as the zero sublevel set of a smooth function. The potential component (17), albeit formally different, produces the same effect of the virtual potential introduced in [6], which goes to infinity as the inverse of a known scalar-valued analytic function in the close vicinity of an obstacle and decays to zero at some positive level surface sufficiently far from the obstacle. Such approach is, in turn, based on the obstacle-avoidance technique introduced long before in [21] under the acronym FIRAS (Force Inducing an Artificial Repulsion from a Surface).

The function (17) may equivalently be written as $B_{\mathrm{M}}(R) := -K_{\mathrm{M}} \log(\mathrm{tr}(R\, e_{\mathrm{BA}} e_{\mathrm{M}}^{\top}) - \cos\theta_{\mathrm{M}})$, where tr denotes matrix trace. Now, in order to compute the Riemannian gradient of such matrix-to-scalar function, it pays to recall the formula

$$\nabla_R B = R\sigma\left(R^{\top}\frac{\partial B}{\partial R}\right), \tag{18}$$

where $\sigma : \mathbb{R}^{3\times 3} \to \mathfrak{so}(3)$ is a matrix-to-matrix function defines as $\sigma(Y) := \frac{1}{2}(Y - Y^{\top})$ that represents an orthogonal projection over the space of skew-symmetric matrices, while the symbol $\frac{\partial}{\partial R}$ denotes the ordinary Jacobian matrix. (It is compelling to specify that the expression (18) holds under the assumption that the tangent bundle $T\mathrm{SO}(3)$ is endowed with the canonical inner product $\langle V_1, V_2\rangle_R := \mathrm{tr}(V_1^{\top} V_2)$ for every $V_1, V_2 \in T_R\mathrm{SO}(3)$.)

In the present case, we got

$$\frac{\partial B_{\mathrm{M}}}{\partial R} = -\frac{K_{\mathrm{M}}}{e_{\mathrm{M}}^{\top} R\, e_{\mathrm{BA}} - \cos\theta_{\mathrm{M}}} e_{\mathrm{M}} e_{\mathrm{BA}}^{\top}. \tag{19}$$

Therefore, the torque component corresponding to a mandatory-type barrier potential takes the expression

$$-R^{\top}\nabla_R B_{\mathrm{M}} = \frac{K_{\mathrm{M}}}{e_{\mathrm{M}}^{\top} R\, e_{\mathrm{BA}} - \cos\theta_{\mathrm{M}}} \sigma(R^{\top} e_{\mathrm{M}} e_{\mathrm{BA}}^{\top}). \tag{20}$$

Likewise, given a forbidden direction $e_{\mathrm{F}} \in \mathbb{R}^3$ expressed in the reference system $\mathcal{F}_{\mathrm{I}}$ and an axis of the spacecraft $e_{\mathrm{BS}} \in \mathbb{R}^3$ expressed in the reference system $\mathcal{F}_{\mathrm{C}}$, the cosine of the angle between these two directions is given by $e_{\mathrm{F}}^{\top} R\, e_{\mathrm{BS}}$. In order to make sure that the axis e_{BS} keeps at an angular distance from the mandatory direction e_{F} larger than a prescribed threshold θ_{F}, the following constraint needs to be imposed

$$\cos\theta_{\mathrm{F}} - e_{\mathrm{F}}^{\top} R\, e_{\mathrm{BS}} > 0. \tag{21}$$

(For comparison purpose let's recall, e.g. from [17], that such constraint written on the basis of a quaternion $[q^{\top}\ q_0]^{\top}$ would read

$$\cos\theta_{\mathrm{F}} - (q_0^2 - q^{\top} q) e_{\mathrm{F}}^{\top} e_{\mathrm{BS}} - 2 e_{\mathrm{F}}^{\top} q q^{\top} e_{\mathrm{BS}} - 2 e_{\mathrm{F}}^{\top} q_0 q^{\times} e_{\mathrm{BS}} > 0,$$

where q_0 denotes the real part of the quaternion and the operator $(\cdot)^{\times}$ returns a $\mathfrak{so}(3)$ matrix from a $\mathbb{R}^3$ vector. Notice that the Jet Propulsion Laboratory (JPL) convention is used to denote quaternions as is customary in the aerospace domain.)

A barrier potential to secure adherence to such directional constraint reads

$$B_{\mathrm{F}}(R) := -K_{\mathrm{F}} \log(\cos\theta_{\mathrm{F}} - \mathrm{tr}(R\, e_{\mathrm{BS}} e_{\mathrm{F}}^{\top})), \tag{22}$$

where $K_{\mathrm{F}} > 0$ determines the strength of the corresponding torque term in the control action. The torque component corresponding to such a forbidden-type barrier potential takes the expression

$$-R^{\top}\nabla_R B_{\mathrm{F}} = \frac{K_{\mathrm{F}}}{e_{\mathrm{M}}^{\top} R\, e_{\mathrm{BS}} - \cos\theta_{\mathrm{F}}} \sigma(R^{\top} e_{\mathrm{F}} e_{\mathrm{BS}}^{\top}). \tag{23}$$

Gluing all pieces together, the complete additive potential expression reads

$$\begin{aligned} V_{\mathrm{ADD}}(R) = &-\frac{1}{2}K_{\mathrm{A}}\ell^2 \exp\left(-\frac{d^2(R_{\mathrm{d}},R)}{\ell^2}\right) - K_{\mathrm{M}}\sum_i \log(e_{\mathrm{M},i}^\top R\, e_{\mathrm{BA}} - \cos\theta_{\mathrm{M},i}) \\ &- K_{\mathrm{F}}\sum_i \log(\cos\theta_{\mathrm{F},i} - e_{\mathrm{F},i}^\top R\, e_{\mathrm{BS}}). \end{aligned} \tag{24}$$

The corresponding control torque term $T_{\mathrm{ADD}}(R) := -R^\top \nabla_R V_{\mathrm{ADD}}(R)$ reads

$$\begin{aligned} T_{\mathrm{ADD}}(R) = &-K_{\mathrm{A}} \exp\left(-\frac{d^2(R_{\mathrm{d}},R)}{\ell^2}\right) \mathrm{Log}(R_{\mathrm{d}}^\top R) + \sum_i \frac{K_{\mathrm{M}}}{e_{\mathrm{M},i}^\top R\, e_{\mathrm{BA}} - \cos\theta_{\mathrm{M},i}} \sigma(R^\top e_{\mathrm{M},i} e_{\mathrm{BA}}^\top) \\ &+ \sum_i \frac{K_{\mathrm{F}}}{e_{\mathrm{F},i}^\top R\, e_{\mathrm{BS}} - \cos\theta_{\mathrm{F},i}} \sigma(R^\top e_{\mathrm{F},i} e_{\mathrm{BS}}^\top), \end{aligned} \tag{25}$$

where summations run over the number of mandatory/forbidden constraints, respectively. We have chosen to weight the mandatory terms with the same constant K_{M} and all forbidden terms with the same constant K_{F}, although, in practice, every coefficients may be chosen to take a different value.

It is interesting, and perhaps counter-intuitive, to notice that the torques corresponding to mandatory-type constraints look alike the terms corresponding to forbidden-type constraints. However, the scalar coefficients in the former types of constraints are positive-valued, while the coefficients in the latter types are negative-valued, hence they behave in an opposite way.

An important aspect to evaluate is the expression of the potential function $\bar{V}_{\mathrm{ADD}}$ and of the corresponding gradient-based torque component $\bar{T}_{\mathrm{ADD}} = -R_{\mathrm{d}}^\top [\nabla_R V_{\mathrm{ADD}}]_{R=R_{\mathrm{d}}}$ at the expected equilibrium point. Calculations show that

$$\begin{cases} \bar{V}_{\mathrm{ADD}} = -\frac{1}{2}K_{\mathrm{A}}\ell^2 - K_{\mathrm{M}}\sum_i \log(e_{\mathrm{M},i}^\top R_{\mathrm{d}}\, e_{\mathrm{BA}} - \cos\theta_{\mathrm{M},i}) - K_{\mathrm{F}}\sum_i \log(\cos\theta_{\mathrm{F},i} - e_{\mathrm{F},i}^\top R_{\mathrm{d}}\, e_{\mathrm{BS}}), \\ \bar{T}_{\mathrm{ADD}} = \sum_i \frac{K_{\mathrm{M}}}{e_{\mathrm{M},i}^\top R_{\mathrm{d}} e_{\mathrm{BA}} - \cos\theta_{\mathrm{M},i}} \sigma(R_{\mathrm{d}}^\top e_{\mathrm{M},i} e_{\mathrm{BA}}^\top) + \sum_i \frac{K_{\mathrm{F}}}{\cos\theta_{\mathrm{F},i} - e_{\mathrm{F},i}^\top R_{\mathrm{d}} e_{\mathrm{BS}}} \sigma(R_{\mathrm{d}}^\top e_{\mathrm{F},i} e_{\mathrm{BS}}^\top), \end{cases} \tag{26}$$

since $d(R_{\mathrm{d}}, R_{\mathrm{d}}) = 0$ and $\mathrm{Log}(R_{\mathrm{d}}^\top R_{\mathrm{d}}) = 0$. The expression $\bar{V}_{\mathrm{ADD}}$ is useful in numerical simulation to verify as to whether the gradient-based control algorithm seeks in fact the minimum of the potential function.

The expression $\bar{T}_{\mathrm{ADD}}$ tells that even at the equilibrium point there exists a non-zero torque that tend to orient the spacecraft in a direction that is not exactly the desired one. In formal terms, the solution of the equation $T_{\mathrm{ADD}}(R) = 0$ differs from $R = R_{\mathrm{d}}$ because of the residual pull-push effect of the barriers. This effect is not necessarily disruptive for at least two reasons: 1) during reorientation, even if the boresight of a telescope does not match exactly the preferred direction of observation of a target, an observation mission might still be carried out; 2) during docking, a tolerance in the alignment might be borne [40] (as in underwater missions [15]).

With the aim of fixing the above-noted inconsistency, the next section 5.3 explains a different approach to the problem.

5.3 Mixed multiplicative-additive potential and related gradient

Many potential functions have been evaluated for the case. Existing approaches differ on how to combine reorientation goal and constraints to concur in the definition of a virtual potential. To recall a few, the paper [24] suggest a mixed multiplicative/additive potential, where the component associated to re-orientation is multiplies by the sum of the barrier-type components associated to directional obstacles. The paper [17] follows a similar approach, although the components associated to re-orientation and obstacles differ in mathematical structure. The paper [30] remarks that a combination of partial potentials may yield a function with potentially multiple critical points and recall the notion of 'navigation functions' which constitute possible remedies to such difficulty. The function proposed in [30] is a nonlinear combination of the reorientation potential and of the sum of the reorientation-potential with the product of constraint-enforcing potentials.

In the present research project, it is deemed appropriate to explore the features of a mixed potential inspired by the paper [24]. Such mixed potential is a variant of the additive potential expressed in (11) and reads

$$V_{\mathrm{MIX}}(R) := A(R) + M(R) \sum_i B_i(R), \tag{27}$$

where the barrier functions take the same expression as in (17) and (22), the attractive function $A(R)$ takes the same expression as in (13) while the additive potential is taken as a quadratic function as

$$M(R) := -\tfrac{1}{2} d^2(R, R_{\mathrm{d}}), \tag{28}$$

which is a monotonically increasing function with one minimum in $R = R_{\mathrm{d}}$.

The detailed expression of the mixed-form potential reads

$$\begin{aligned} V_{\mathrm{MIX}}(R) = &- \frac{1}{2} K_{\mathrm{A}} \ell^2 \exp\left(-\frac{d^2(R, R_{\mathrm{d}})}{\ell^2}\right) \\ &- \frac{1}{2} d^2(R, R_{\mathrm{d}}) \left(K_{\mathrm{M}} \sum_i \log(e_{\mathrm{M},i}^\top R\, e_{\mathrm{BA}} - \cos\theta_{\mathrm{M},i}) + K_{\mathrm{F}} \sum_i \log(\cos\theta_{\mathrm{F},i} - e_{\mathrm{F},i}^\top R\, e_{\mathrm{BS}}) \right). \end{aligned} \tag{29}$$

The torque control component corresponding to the Riemannian gradient of such virtual potential may be determined by going through the same calculations shown in Section 5.2. The obtained expression $T_{\mathrm{MIX}}(R) := -R^\top \nabla_R V_{\mathrm{MIX}}(R)$ reads

$$\begin{aligned} T_{\mathrm{MIX}} = &- K_{\mathrm{A}} \exp\left(-\frac{d^2(R, R_{\mathrm{d}})}{\ell^2}\right) \mathrm{Log}(R_{\mathrm{d}}^\top R) \\ &+ \left(K_{\mathrm{M}} \sum_i \log(e_{\mathrm{M},i}^\top R\, e_{\mathrm{BA}} - \cos\theta_{\mathrm{M},i}) + K_{\mathrm{F}} \sum_i \log(\cos\theta_{\mathrm{F},i} - e_{\mathrm{F},i}^\top R\, e_{\mathrm{BS}}) \right) \mathrm{Log}(R_{\mathrm{d}}^\top R) \\ &+ \frac{1}{2} d^2(R, R_{\mathrm{d}}) \left(\sum_i \frac{K_{\mathrm{M}}}{e_{\mathrm{M},i}^\top R\, e_{\mathrm{BA}} - \cos\theta_{\mathrm{M},i}} \sigma(R^\top e_{\mathrm{M},i} e_{\mathrm{BA}}^\top) + \sum_i \frac{K_{\mathrm{F}}}{e_{\mathrm{F},i}^\top R\, e_{\mathrm{BS}} - \cos\theta_{\mathrm{F},i}} \sigma(R^\top e_{\mathrm{F},i} e_{\mathrm{BS}}^\top) \right). \end{aligned} \tag{30}$$

With reference to the classical error-feedback control, it is worth noticing that the above expression appears as a weighted sum of the reorientation error $E := \mathrm{Log}(R_{\mathrm{d}}^\top R)$ and of a constraint-enforcing torque

$$C := \sum_i \frac{K_{\mathrm{M}}}{e_{\mathrm{M},i}^\top R\, e_{\mathrm{BA}} - \cos\theta_{\mathrm{M},i}} \sigma(R^\top e_{\mathrm{M},i} e_{\mathrm{BA}}^\top) + \sum_i \frac{K_{\mathrm{F}}}{\cos\theta_{\mathrm{F},i} - e_{\mathrm{F},i}^\top R\, e_{\mathrm{BS}}} \sigma(R^\top e_{\mathrm{F},i} e_{\mathrm{BS}}^\top) \tag{31}$$

through the weighting functions

$$W := -K_{\mathrm{M}} \sum_i \log(e_{\mathrm{M},i}^\top R\, e_{\mathrm{BA}} - \cos\theta_{\mathrm{M},i}) - K_{\mathrm{F}} \sum_i \log(e_{\mathrm{F},i}^\top R\, e_{\mathrm{BS}} - \cos\theta_{\mathrm{F},i}) \tag{32}$$

and M, respectively to which we added an attractive potential A to enforce the satellite to reach the desired R_{d}.

It is immediate to recognize that, at the sought equilibrium point $R = R_{\mathrm{d}}$, it holds that $V_{\mathrm{MIX}}(R_{\mathrm{d}}) = 0$ and, more importantly, that $T_{\mathrm{MIX}}(R_{\mathrm{d}}) = 0$. Such approach might potentially be able to overcome the problem of non-zero torque at equilibrium entailed by the approach presented in Section 5.2. The virtual potential (29) may be interpreted as an additive repulsive potential *weighted* by an additive potential increasing with the distance to the desired attitude.

The reason why an attractive function A has been added to the equation is that a potential drawback of the mixed multiplicative-additive approach just detailed could be that there is no chance to balance, through a weighting constant, the opposed actions of the attractive term and of the repulsive terms.

5.4 Relation with a navigation function

The barrier terms, on which the above-discussed virtual potential functions are based on, may be recast in a different expression by exploiting the properties of the logarithm. In fact, upon defining the total barrier term

$$B_{\mathrm{T}} := K_{\mathrm{M}} \sum_i \log(e_{\mathrm{M},i}^{\top} R\, e_{\mathrm{BA}} - \cos\theta_{\mathrm{M},i}) + K_{\mathrm{F}} \sum_i \log(\cos\theta_{\mathrm{F},i} - e_{\mathrm{F},i}^{\top} R\, e_{\mathrm{BS}}), \tag{33}$$

it is immediate to recognize that

$$\begin{aligned} B_{\mathrm{T}} &= \sum_i \log(e_{\mathrm{M},i}^{\top} R\, e_{\mathrm{BA}} - \cos\theta_{\mathrm{M},i})^{K_{\mathrm{M}}} + \sum_i \log(\cos\theta_{\mathrm{F},i} - e_{\mathrm{F},i}^{\top} R\, e_{\mathrm{BS}})^{K_{\mathrm{F}}} \\ &= \log\left(\prod_i (e_{\mathrm{M},i}^{\top} R\, e_{\mathrm{BA}} - \cos\theta_{\mathrm{M},i})^{K_{\mathrm{M}}} \prod_i (\cos\theta_{\mathrm{F},i} - e_{\mathrm{F},i}^{\top} R\, e_{\mathrm{BS}})^{K_{\mathrm{F}}} \right). \end{aligned} \tag{34}$$

It readily follows that

$$\exp(B_{\mathrm{T}}) = \prod_i \prod_j (e_{\mathrm{M},i}^{\top} R\, e_{\mathrm{BA}} - \cos\theta_{\mathrm{M},i})^{K_{\mathrm{M}}} (\cos\theta_{\mathrm{F},j} - e_{\mathrm{F},j}^{\top} R\, e_{\mathrm{BS}})^{K_{\mathrm{F}}}. \tag{35}$$

Hence the total barrier function may be regarded as a product of partial function that are positive only in the permissible zones delimited by each barrier, a design strategy suggested in [30], where the weighting coefficients K_{M} and K_{F} play the role of order parameters.

Position control

During cruising and docking under positional constraints

Autonomous navigation toward the space station aimed at complete docking is one of the primary goals of control design. Since navigation is a complex task, it is customary to break it into subtasks [4] to be separately tackled on the basis of the current physical distance between the spacecraft and the docking port. In the present research project, the approaching trajectory is subdivided in three parts: cruising, far-end docking and near-end docking, as detailed in the next sections. Figure 8 serves to display Juno's trajectory for its mission, in this case docking is not comprehended but the image clearly shows how the spacecraft moves between different orbits which is a similar behavior as the chaser's in this paper that needs to go from a lower orbit to a higher orbit (the same as the station) before attempting docking.

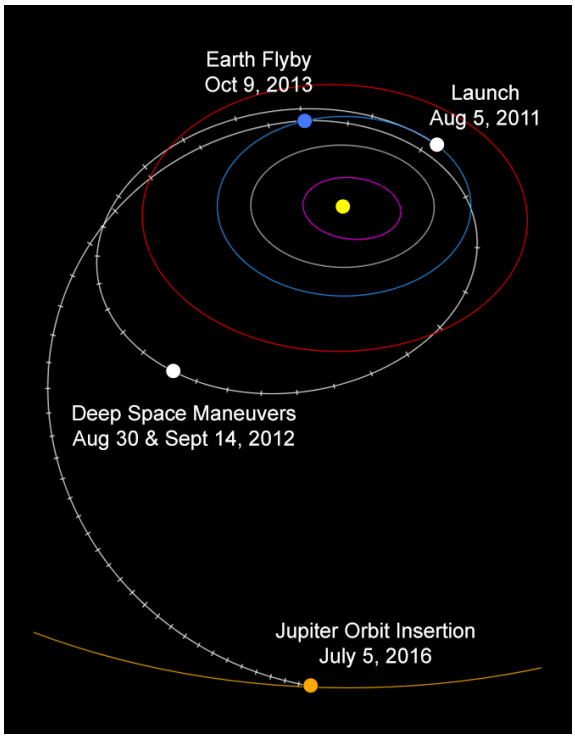

Figure 8: Spacecraft Juno's mission trajectory via: https://www.jpl.nasa.gov

5.5 Control strategy during cruising in the presence of physical obstacles

The maneuvering a spacecraft in the presence of obstacles requires to be carried out autonomously by the help of sensors by a guidance algorithm. The algorithm devised in the present project is based on virtual attractive-repulsive potential theory and is declined in three versions: a version adapted from [4], a version based on impulsive control drawn from [27], and a version that build on impulsive control by an adaptive desired speed.

During an approaching phase, the motion of the spacecraft is referred to the station's LVLH reference system, hence the attitude matrix R, in the present context, is the one that aligns the spacecraft-fixed reference frame $\mathcal{F}_{\mathrm{C}}$ to the station-fixed reference frame $\mathcal{F}_{\mathrm{S}}$.

According to [4], the control algorithm switches on the thrusters according to a first-order

sliding-mode control method, described by the relation:

$$f_{\mathrm{rt}} = -2\,\varphi\,\bar{f}_{\mathrm{rt}}\,R\,\mathrm{sign}(\sigma), \tag{36}$$

which expresses the fact that a pair of thrusters per axis of the spacecraft are eventually switched on, hence exert a thrust twice as large as the maximum thrust. Which pairs of thrusters is currently switched on is determined by the sliding output vector $\sigma \in \mathbb{R}^3$, whose value is inessential except for the signs of its components. The variable $\varphi \in \{0, 1\}$ represents a flag employed in impulsive control.

In general, sliding mode control (SMC) is based on a discontinuous feedback that switches among a number of control laws according to a pre-defined decision rule. For a basic review of its features, readers might consult [1, 37]. For a more advanced account of SMC, interested readers might consult [39].

It is worth highlighting that the force term f_{rt} and the number n are related through the relation

$$\varphi\,\|f_{\mathrm{rt}}\|^2 = 2\,n\,\bar{f}_{\mathrm{rt}}^2, \tag{37}$$

which, in fact, allows determining the number of active thrusters on the basis of the output of the control algorithm.

The variable σ depends on the mismatch between the current velocity $\dot{p}$ of the spacecraft and the desired velocity $\dot{p}_{\mathrm{d}} \in \mathbb{R}^3$, as well as on the mismatch between the current position p of the spacecraft and the desired position $p_{\mathrm{d}} \in \mathbb{R}^3$, through the linear combination

$$\sigma := \dot{p} - \dot{p}_{\mathrm{d}} + c(p - p_{\mathrm{d}}). \tag{38}$$

The constant $c \geq 0$ determines the relative weight between position and velocity mismatch.

The quantity p_{d} is determined by the position of the target of the cruising phase, which normally is located from within a few hundreds to a few dozens meters away from the docking port, and is generally constant. The desired velocity changes along the trajectory and is determined through a virtual potential by the following expression

$$\dot{p}_{\mathrm{d}} = v_{\mathrm{d}}\,\frac{-\nabla_p V_{\mathrm{C}}}{\|\nabla_p V_{\mathrm{C}}\|}, \tag{39}$$

where $v_{\mathrm{d}} > 0$ denotes the desired speed, determined independently of the virtual potential, while $\nabla_p V_{\mathrm{C}} \in \mathbb{R}^3$ denotes the gradient of the potential $V_{\mathrm{C}} : \mathbb{R}^3 \to \mathbb{R}$. As a result, it holds that $\|\dot{p}_{\mathrm{d}}\| = v_{\mathrm{d}}$, hence the entity and the direction of the desired speed are determined independently by the control algorithm.

The cruising phase ends when the distance between the spacecraft and the desired position is less than a given threshold, namely as soon as $\|p - p_{\mathrm{d}}\| \leq 50$.

5.6 Virtual potential design

The virtual potential function is designed to decrease when a spacecraft gets closer to the target location and to increase when a spacecraft gets closer to a physical obstacle. The gradient-based sliding-mode control algorithm is hence designed to seek the minimum of the potential function.

The virtual potential is constructed as a sum of terms, one of which is attractive and depends on the desired location, while further terms are repulsive and depend on the location and on the safety radii of physical obstacles. Formally, the potential reads

$$V_{\mathrm{C}}(p) = A_{\mathrm{C}}(p) + \sum_i P_{\mathrm{C},i}(p), \tag{40}$$

where $A_{\mathrm{C}} : \mathbb{R}^3 \to \mathbb{R}$ denotes the attractive-type component and $P_{\mathrm{C},i} : \mathbb{R}^3 \to \mathbb{R}$ denote the repulsive-type components. The sum runs over the number of obstacles within the radius of sensitivity of the proximity sensors aboard the spacecraft.

The attractive-type component of the potential function is defined by

$$A_{\mathrm{C}}(p) := \tfrac{1}{2} H_{\mathrm{A}} \|p - p_{\mathrm{d}}\|^2, \tag{41}$$

where $H_{\mathrm{A}} > 0$ is a constant that determines the strength of the attractive component of the potential. The component $A_{\mathrm{C}}(p)$ is monotonically increasing with a unique minimum in $p = p_{\mathrm{d}}$.

In order to enable the spacecraft to avoid the physical obstacles, a number of repulsive-type components need to be designed that exhibit their maximum value in correspondence of the location of the obstacles and whose action vanish as rapidly as the distance between the spacecraft and the obstacles increases. We shall denote as $o_i \in \mathbb{R}^3$ the location of each obstacle in the station-fixed reference frame $\mathcal{F}_{\mathrm{S}}$ and by η_i the safety radius of each obstacle. Obstacles are assumed to be of spherical shape, hence each safety radius may be thought of as the sum of the radius of the spherical obstacle augmented by an extra safety distance (which should not exceed the sensitivity radius of the proximity sensor). On the basis of such data, the repulsive-type component of the potential associated to the i^{th} obstacle was defined as

$$P_{\mathrm{C},i}(p) := \frac{1}{2} H_{\mathrm{R}} \exp\left(-\frac{\|p - o_i\|^2}{\eta_i^2}\right), \tag{42}$$

where the constant $H_{\mathrm{R}} > 0$ determines the strength of each repulsive term. Notice that the expression chosen represents only a soft constraint: although it cannot be ensured that the spacecraft will not enter the obstacle, a reasonable safety distance may be determined through a careful handcrafting of the safety radii.

The anti-gradient of the virtual potential function reads

$$-\nabla_p V_{\mathrm{C}} = -H_{\mathrm{A}}(p - p_{\mathrm{d}}) + H_{\mathrm{R}} \sum_i \exp\left(-\frac{\|p - o_i\|^2}{\eta_i^2}\right) \frac{p - o_i}{\eta_i^2}. \tag{43}$$

It is important to remark that the present setting stays unvaried whether the obstacles are fixed with respect to the reference frame $\mathcal{F}_{\mathrm{S}}$ or are moving, instead.

5.7 Speed intensity determination

The desired speed may be determined on the basis of different criteria. In the present research work are compared the performances of three strategies to determine such speed.

The computationally-simplest strategy was drawn from reference [4] and consists in setting the desired speed to the maximum allowable speed $\bar{v}$ and the flag φ to 'on'-state, namely

$$v_{\mathrm{d}} = \bar{v}, \ \varphi = 1. \tag{44}$$

The next strategy examined was inspired by the notion of impulsive control discussed in [27]. It consists in switching on the reaction thrusters only when the spacecraft effectively gets off the right track, hence keeping them in the off state whenever not necessary, with the aim to save propellant. Formally,

$$v_{\mathrm{d}} = \bar{v}, \ \varphi = \begin{cases} 1, & \text{if } \Delta\xi > \tau \\ 0, & \text{otherwise,} \end{cases} \tag{45}$$

where $\Delta\xi := \left\| \frac{\dot{p}}{\|\dot{p}\|} - \frac{\nabla_p V_{\mathrm{C}}}{\|\nabla_p V_{\mathrm{C}}\|} \right\|$ and τ denotes a predefined threshold that determines the sensitivity of the algorithm to difference in direction. By handcrafting and testing the model was found that the threshold should be of the order of 10^{-2} for example using $\tau = 0.05$. Notice that this strategy only influences the 'off'-state of the thrusters, while does not influence the 'on'-state.

An allegedly more proficient strategy also influences the 'on'-state of the thrusters by determining the speed amplitude. The law here proposed aims to determine a desired speed in such way so that the more the spacecraft gets closer to the target, the lesser the cruising speed is. In formulas:

$$\begin{cases} v_{\mathrm{d}} = \min\left\{\bar{v}, 5\Delta\xi \|p - p_{\mathrm{d}}\|^{\frac{1}{4}}\right\}, \\ \varphi = \begin{cases} 1, & \text{if } \Delta\xi > \tau \\ 0, & \text{otherwise.} \end{cases} \end{cases} \tag{46}$$

The relationship to determine the desired speed intensity was empirically handcrafted. The hard-limiting check prevents the computed speed to exceed its maximum allowable value.

5.8 Attitude control during a cruising phase

During cruising it is not essential to control the attitude of a spacecraft, which may keep a constant orientation, resulting from previous maneuvers, until the beginning of the docking phase. This statement can be made provided that the spacecraft has a sufficient number of sensors on board to detect the presence of obstacles whatever the attitude is and also that the attitude maintained favors connection to ground station. Nevertheless, to aid stability of a spacecraft [4] against unforeseen events, in the present research projects it was deemed appropriate to explore attitude regulation strategies.

A way to control orientation during cruising is to establish a desired attitude R_{d} and to set up a control strategy to make sure the actual attitude matrix R of the spacecraft matches the desired attitude. In order to control the attitude of the spacecraft, a control torque is chosen according to synchronization theory [13] to be

$$T_{\mathrm{rw}} := -\,\mathbb{Q}\Omega - K_{\mathrm{f}}\,\Omega - K_{\mathrm{S}}\log(R_{\mathrm{d}}^{\top}R), \tag{47}$$

where $K_{\mathrm{S}} > 0$ determines the strength of coupling in the leader/follower pair. (Notice that the term $K_{\mathrm{S}}\log(R_{\mathrm{d}}^{\top}R)$ stems as the Riemannian gradient ∇_R of the potential function $\frac{1}{2}K_{\mathrm{S}}\,d^2(R,R_{\mathrm{d}})$ and may be recognized as the 'proportional' component of a Lie-group type PID controller.)

To what concerns the desired attitude, two possibilities were studied. A first attempt consists in setting up a fixed attitude matrix that coincides with the one required for docking, namely $R_{\mathrm{d}} = I_3$. As a second attempt, the desired attitude was set up to the one which corresponds to the direction of the desired speed $\dot{p}_{\mathrm{d}}$ as defined in (39). The relation between the (time-varying) matrix R_{d} and the components of the desired speed vector $\dot{p}_{\mathrm{d}}$ may be found in [4], in equations (15)-(17).

A third strategy, corresponding to lack of synchronization, was tested against the former two methods. This corresponds to setting the control torque as

$$T_{\mathrm{rw}} := -\,\mathbb{Q}\Omega - K_{\mathrm{f}}\,\Omega, \tag{48}$$

which aims at just passivating the spacecraft and to mitigate the effects of unpredictable disturbances in other words the spacecraft is instructed to activate its reaction wheels to reorient the spacecraft in the wanted direction for example if the spacecraft gets hit by very small debris.

A fourth strategy, loosely based on [12], consists in setting up a control torque that tends to align the speed $\dot{p}$ of the spacecraft to the desired speed resulting from the virtual potential function described in Section 5.5, namely $-\frac{\nabla_p V_{\mathrm{C}}}{\|\nabla_p V_{\mathrm{C}}\|}$. The corresponding torque term reads

$$T_{\mathrm{rw}} := -\,\mathbb{Q}\Omega - K_{\mathrm{f}}\,\Omega + \frac{K_{\mathrm{FBP}}}{\|\nabla_p V_{\mathrm{C}}\|}(\dot{p}(\nabla_p V_{\mathrm{C}})^{\top} - (\nabla_p V_{\mathrm{C}})\dot{p}^{\top}), \tag{49}$$

where $K_{\mathrm{FBP}} > 0$ denotes the aligning torque. Notice that the rightmost terms corresponds to the cross product $\dot{p}\wedge(\nabla_p V_{\mathrm{C}})$ in $\mathfrak{so}(3)$, which vanishes when these vectors are parallel.

5.9 Final guidance to docking in the absence of physical obstacles

In close proximity to the space station, at a distance of a few dozen meters, it is reasonable and safe to assume that no large obstacles stand in the way to the space station. During the final approach maneuver, therefore, the only obstacle to be taken into account is the outer structure of the space station itself. The space station (let's refer to the ISS) in fact has various modules with different shapes that need to be avoided during the final approach as well as a number of robotic arms 9 to complete various actions like docking, moving personal during missions or maintenance and rearranging payload across the station. As of the current date, the ISS main robotic arms are Canadarm2 and the European Robotic Arm (ERA), however, in future launches is planned to augment the station's capabilities with additional robotic arms such as "GITAI S1" designed in Japan that is now undergoing the testing phase .

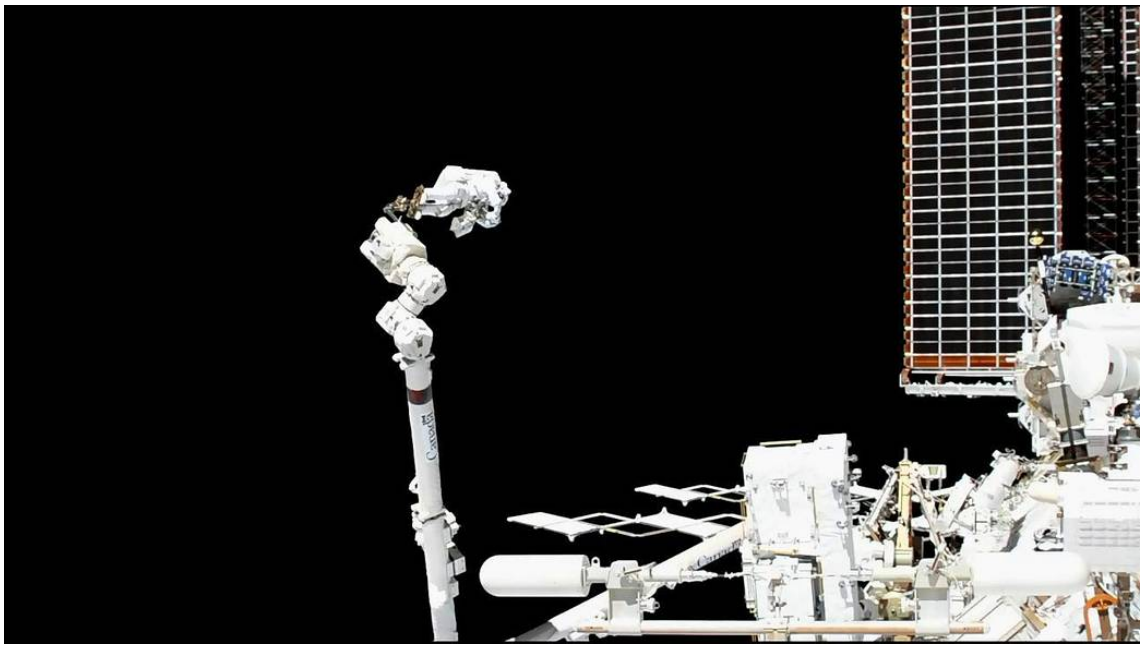

Figure 9: Station Commander Luca Parmitano of the European Space Agency conducts repairs while attached to the space station's robotic arm during the first spacewalk to repair the Alpha Magnetic Spectrometer on Nov. 15, 2019 source: nasa.gov

In order to avoid colliding with any part of the station, a technique adapted from [27] is deployed, based on a safety zone whose border takes the shape of a cardioid curve. The radius of the cardioid must be selected in such a way to encompass the whole space station in order to allow a spacecraft to safely approach from every direction. The cardioid itself includes a recess, a cuspid whose tip coincides with the docking port and whose asymptote coincides with the docking axes (taken to be the X axis of the LVLH reference frame). The actual maneuver during docking is divided into two subtasks.

The first subtask is termed *far-end approaching*. It ensures that, not matter what is the direction of arrival of the spacecraft, it gets positioned to the right of the docking port while avoiding the outskirts of the space station by keeping out of the cardioid-shaped safety region. This procedure takes, as input, the desired location of the just mentioned intermediate step $p_{\text{fe}} \in \mathbb{R}^3$ and the safety radius of the space station, that shall be denotes as r_{S}. The tip of the cardioid cusp is located at $p_{\text{fe}} \in \mathbb{R}^3$ and the cusp opens along the X axis. The far-end approaching phase continues until the distance between the spacecraft and the desired position is less than a given threshold, namely as soon as $\|p - p_{\text{fe}}\| \leq 1$.

The current distance and angle of arrival, in the LVLH reference frame $\mathcal{F}_{\text{S}}$, are calculated as

$$\begin{cases} \rho = \|p - p_{\text{fe}}\|, \\ \theta = \frac{\pi}{2} - \text{atan2}((p - p_{\text{fe}})^\top e_{\text{x}}, -(p - p_{\text{fe}})^\top e_{\text{z}}), \end{cases} \tag{50}$$

where the function atan2(·) returns the correct and unambiguous value for the angle while converting from Cartesian coordinates to polar coordinates.

The cardioid is built from its parametric equations and a preferred direction is evaluated at each position during the far-end phase from the boundary tangent vector of the cardioid

$$\gamma_{\text{fe}} = \begin{cases} \dot{x} = -H_{\text{t}}(\sin(\theta) - \sin(2\theta)), \\ \dot{y} = 0, \\ \dot{z} = -H_{\text{t}}(\cos(\theta) - \cos(2\theta)), \end{cases} \tag{51}$$

where $H_{\text{t}} > 0$ is the weighting factor that can be handcrafted *ad hoc*. The control strategy used to achieve the task is a variable desired speed control similar to the one described from the cruising phase 5.7

$$\begin{cases} v_{\text{d}} = \min\left\{\bar{v}_{\text{fe}}, \Delta\xi\rho^{\frac{1}{4}}\right\}, \\ \varphi = \begin{cases} 1, & \text{if } \Delta\xi > \tau \\ 0, & \text{otherwise.} \end{cases} \end{cases} \tag{52}$$

where $\Delta\xi := \left\| \frac{\dot{p}}{\|\dot{p}\|} - \frac{\gamma_{\text{fe}}}{\|\gamma_{\text{fe}}\|} \right\|$ and $\bar{v}_{\text{fe}} = \frac{\bar{v}}{10}$ were chosen empirically after evaluating some real cases of docking maneuvers.

The second subtask is termed *near-end approaching*, it ensures slow and steady docking in the absence of any obstacle of sort, except for the docking port. Such procedure takes, as input, the desired location $p_{\text{ne}} \in \mathbb{R}^3$ to drive the spacecraft to the docking port. Since the spacecraft is now aligned with the docking axis, the preferred direction is defined as

$$\gamma_{\text{ne}} = -e_{\text{x}}, \tag{53}$$

during the entirety of the phase.

The control strategy used in this phase is a variable desired speed control as described before but considering instead a non-impulsive control, this choice was taken due to the necessity to have the best level of precision possible while in the previous phases the margin of error was larger. This requirement is due both to the proximity of the space station's modules and arms as well as the level of accuracy needed to align the chaser to the docking port so that once the maneuver is over the *soft* and *hard* docking can be carried out [3]. In formulas the desired speed reads:

$$v_{\text{d}} = \min\{\bar{v}_{\text{ne}}, \Delta\xi\rho^{\frac{1}{4}}\}, \tag{54}$$

where $\Delta\xi := \left\| \frac{\dot{p}}{\|\dot{p}\|} - \frac{\gamma_{\text{ne}}}{\|\gamma_{\text{ne}}\|} \right\|$, $\rho := \|p - p_{\text{ne}}\|$ and $\bar{v}_{\text{ne}} = \bar{v}_{\text{fe}}$.

The near-end approaching phase continues until the distance between the spacecraft and the desired position is ideally zero, especially considering the position p of the spacecraft as the position of its center of mass, we can define the end of this phase when that distance is equal to the distance between the center of mass and the juncture port of the spacecraft.

[3] The soft docking refers to making contact and latching of the docking connector. After soft docking, an hard docking is completed where it is first checked that both spacecrafts are pressurized and then is formed and airtight seal granting the safe opening of the hatches

5.10 Alignment to a docking axis during final guidance

In order to regulate the attitude of a spacecraft during the final guidance stage, a control torque is again chosen according to synchronization to be

$$T_{\mathrm{rw}} := -\,\mathbb{Q}\Omega - K_{\mathrm{f}}\,\Omega - K_{\mathrm{D}}\log(R_{\mathrm{d}}^{\top} R), \tag{55}$$

with $K_{\mathrm{D}} > 0$.

During final guidance, the desired attitude of the spacecraft is constant to $R_{\mathrm{d}} = I_3$, which describes a state of stable alignment between the reference system $\mathcal{F}_{\mathrm{C}}$ and the frame $\mathcal{F}_{\mathrm{S}}$. Hence, the expression of the active torque may be simplified to

$$T_{\mathrm{rw}} = -\,\mathbb{Q}\Omega - K_{\mathrm{f}}\,\Omega - K_{\mathrm{D}}\log(R). \tag{56}$$

6 Results of numerical experiments

In this section is presented the culmination of the extensive computational investigations with outcomes of the numerical experiments made through systematic simulation, data-driven exploration and extensive handcrafting. The parameters that appear in the mathematical model of a spacecraft motion are summarized in Table 1.

Parameter	Symbol	Value
Initial spacecraft mass	m_0	600 (kg)
Maximum allowable speed	$\bar{v}$	6 (m/s)
Principal inertia	J_{C}	144 (kg·m^2)
Maximum thrust	$\bar{f}_{\mathrm{rt}}$	10 (N)
Frontal area	S	1.44 (m^2)
Drag coefficient	C_{D}	2.20 $(-)$
Specific impulse	I_{sp}	220 (s)
Gravitational acceleration	g	9.81 (m/s^2)
Atmosphere density	ρ	10^{-12} (kg/m^3)
Orbit radius	r	$6,878 \cdot 10^3$ (m)
Gravitational parameter	μ	$3.986 \cdot 10^{14}$ (m^3/s^2)

Table 1: Physical parameters and constants entering the spacecraft model.

6.1 Numerical simulations on reorientation

In order to test the reorientation strategy, the numerical experiments adapted from [24] will be replicated with two different potentials, namely, additive-potential 5.2 and mixed-potential 5.3 that will be later discussed. Since during the testing phase some inconsistencies have been detected in the numerical data, some data has been restored in consistency (the authors, contacted on this matter, have not replied to the inquiry).

In these experiments, the spacecraft is assumed to be endowed with a radio antenna whose boresight axis is $e_{\mathrm{BA}} = e_{\mathrm{y}}$ and a sensor whose boresight axis is $e_{\mathrm{BS}} = e_{\mathrm{z}}$. In order to evaluate the performance of reorientation, it is defined the following figure of merit, referred to as Reorientation Performance Indicator:

$$\mathrm{RPI} := 100 \left(1 - \frac{d(R_{\mathrm{a}}, R_{\mathrm{d}})}{d(R_{\mathrm{i}}, R_{\mathrm{d}})} \right) \ (\%), \tag{57}$$

where R_{a} denotes the attitude actually achieved by the reorientation control algorithm in the given time frame. All experiments in the present section were performed with a stepsize $h = 0.01$ (sec).

In the following experiments, the initial angular speed Ω_0 was set to 0_3 (which denotes a null 3×3 matrix).

Experiment 1: The first experiment consisted in simulating reorientation from an initial attitude, described by the matrix R_{i} to a desired attitude, described by the rotation matrix R_{d}, in the presence of a mandatory zone in which the antenna must always lie within during the process, according to *Case 2* discussed in the paper [24]. The problem will be tackled by an additive-potential-based control algorithm as explained in Section 5.2.

In this experiment, the potential and the associated torque read

$$\begin{cases} V_{\mathrm{ADD}}(R) = & -\frac{1}{2}K_{\mathrm{A}}\ell \exp\left(-\frac{d^2(R_{\mathrm{d}},R)}{\ell}\right) - K_{\mathrm{M}}\log(e_{\mathrm{M}}^{\top}R\,e_{\mathrm{BA}} - \cos\theta_{\mathrm{M}}), \\ T_{\mathrm{ADD}}(R) = & -K_{\mathrm{A}}\exp\left(-\frac{d^2(R_{\mathrm{d}},R)}{\ell}\right)\mathrm{Log}(R_{\mathrm{d}}^{\top}R) + \frac{K_{\mathrm{M}}}{e_{\mathrm{M}}^{\top}R\,e_{\mathrm{BA}}-\cos\theta_{\mathrm{M}}}\sigma(R^{\top}\,e_{\mathrm{M}}\,e_{\mathrm{BA}}^{\top}). \end{cases} \tag{58}$$

Table 2 shows the data pertaining to this simulation tackled with a virtual additive potential.

Description	**Numerical value**
Initial attitude R_{i}	$\begin{bmatrix} 0.3181 & 0.9375 & -0.1409 \\ 0.7050 & -0.3333 & -0.6260 \\ 0.6339 & -0.0998 & 0.7670 \end{bmatrix}$
Desired attitude R_{d}	$\begin{bmatrix} 0.0265 & 0.7821 & 0.6226 \\ 0.2073 & 0.6050 & -0.7688 \\ 0.9779 & -0.1494 & 0.1462 \end{bmatrix}$
Mandatory direction e_{M}	$[0.8530 \;\; -0.2653 \;\; 0.4495]^{\top}$
Aperture of the mandatory cone θ_{M}	70 (°)
Constant K_{A}	$2.8 \cdot 10^{-1} J_{\mathrm{C}}$
Constant ℓ	50
Constant K_{f}	$1.4 J_{\mathrm{C}}$
Constant K_{M}	$1 \cdot 10^{-5} J_{\mathrm{C}}$

Table 2: Numerical data corresponding to *Experiment 1* tackled with a virtual additive potential. The initial and desired attitude are represented using a 3×3 matrix.

The numerical results obtained with an additive potential are illustrated in the Figure 10 while the outcome achieved by the control algorithm in the given time frame is RPI = 100% and the trajectory can be visualized in Figure 11.

As it may be readily appreciated from the figure, the optimization-based control algorithm effectively attains the minimum value of the potential function while keeping the boresight of the antenna within the mandatory cone. It is interesting to point out that, through some handcrafting of the constants, it is possible to operate while being really close to the barrier and reach the goal which assumes importance when acknowledging that operating in such area is difficult because

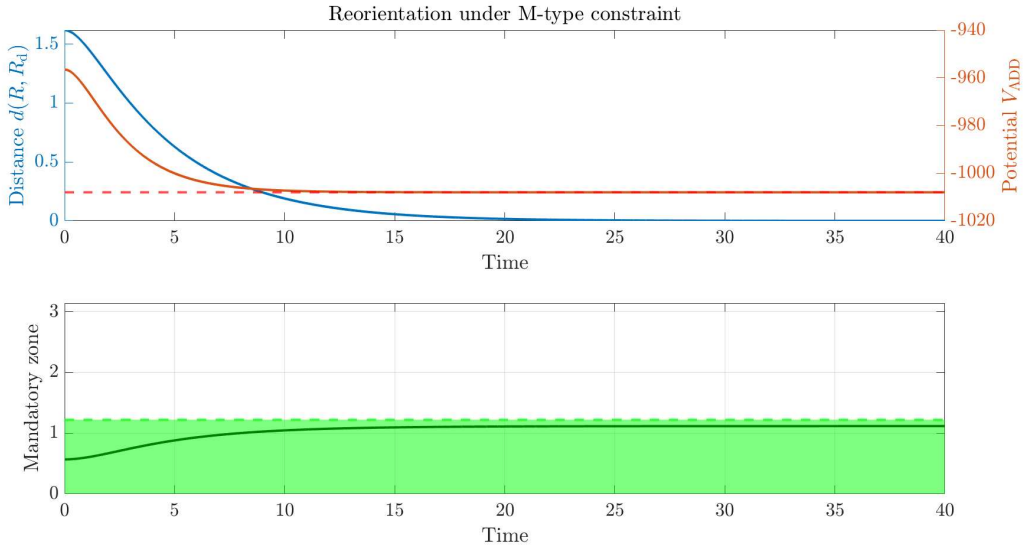

Figure 10: Numerical results obtained for the *Experiment 1*. Top panel: values of the distance between the actual attitude and the desired attitude, and value of the potential during reorientation; the dashed line represents the theoretically-evaluated minimum value of the potential pertaining to this experiment. Bottom panel: Angle between the boresight direction of the antenna and the mandatory direction; the green area represents the mandatory zone. Time is measured in seconds.

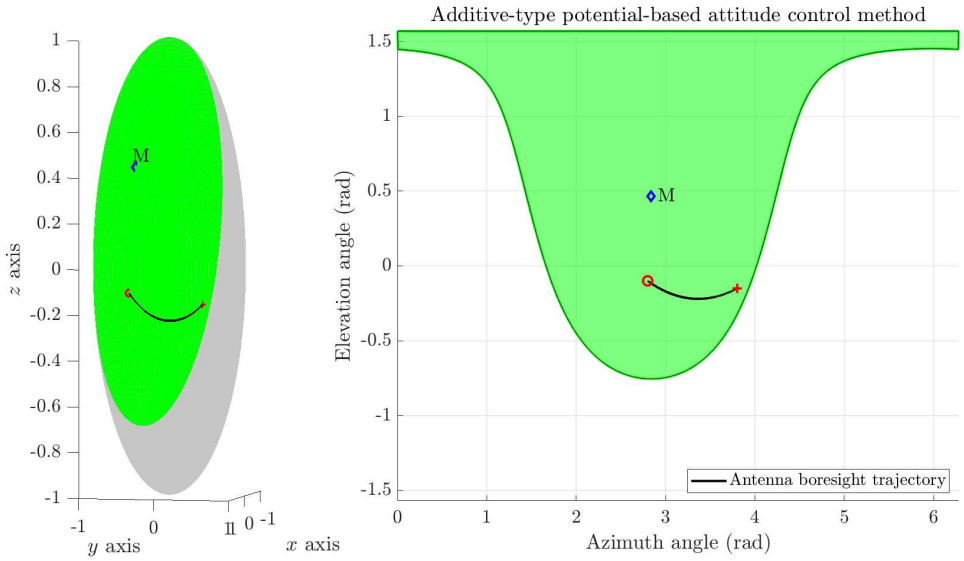

Figure 11: Trajectory achieved by the mandatory axis as explained in *Experiment 1*. Left panel: The trajectory is shown on a sphere that surrounds the satellite and centered in the center of gravity of the spacecraft. Right panel: Two dimensional representation of the sphere, the mandatory zone and the trajectory of the mandatory axis. The red cross represents the attitude reached at the end of the simulation, while the red circle represents the initial attitude.

bounded by two different artificial potential functions namely the attractive one towards the goal and the repulsive one from the barrier.

Experiment 1.1: now a different approach to the same problem will be presented (*Case 2* of paper [24]) that uses a variant of the previously explained potential-based maneuver which is the mixed additive-multiplicative potential-based approach explained in Section 5.3. Let this approach be called mixed-potential-based control from now on. The potential and the associated torque of this experiment read:

$$\begin{cases} V_{\mathrm{MIX}}(R) = & -\frac{1}{2}K_{\mathrm{A}}\ell\exp\left(-\frac{d^2(R_{\mathrm{d}},R)}{\ell}\right) - K_{\mathrm{M}}\frac{d^2(R_{\mathrm{d}},R)}{2}\log(e_{\mathrm{M}}^{\top}R\,e_{\mathrm{BA}} - \cos\theta_{\mathrm{M}}), \\ T_{\mathrm{MIX}}(R) = & -K_{\mathrm{A}}\exp\left(-\frac{d^2(R_{\mathrm{d}},R)}{\ell}\right)\mathrm{Log}(R_{\mathrm{d}}^{\top}R) + K_{\mathrm{M}}\log(e_{\mathrm{M}}^{\top}R\,e_{\mathrm{BA}} - \cos\theta_{\mathrm{M}})\mathrm{Log}(R_{\mathrm{d}}^{\top}R) \\ & + \frac{d^2(R_{\mathrm{d}},R)}{2}\frac{K_{\mathrm{M}}}{e_{\mathrm{m}}^{\top}R\,e_{\mathrm{BA}}^{\top} - \cos\theta_{\mathrm{M}}}\,\sigma(R^{\top}\,e_{\mathrm{M}}\,e_{\mathrm{BA}}^{\top}). \end{cases} \tag{59}$$

The Table 3 shows the data pertaining to this simulation tackled with a virtual mixed potential.

Description	**Numerical value**
Constant K_{A}	$9.3 \cdot 10^{-2} J_{\mathrm{C}}$
Constant ℓ	50
Constant K_{f}	$1.4 J_{\mathrm{C}}$
Constant K_{M}	$0.1 J_{\mathrm{C}}$

Table 3: Numerical data corresponding to the numerical *Experiment 1.1* tackled with a virtual mixed potential. Note that the initial and desired attitude are not shown as they are the same as *Experiment 1* (6.1) as well as the mandatory direction and its aperture of mandatory cone

The numerical results obtained with a mixed potential are illustrated in the Figure 12. The result achieved by the control algorithm in the given time frame is RPI = 100%. By comparing the two approaches that tackle the same problem (Figure 11 vs Figure 13) where the former shows the additive potential case while the latter displays the mixed potential case it can be noticed that the trajectories are not exactly the same but really similar to each other. This, in fact, is a particular case in which the constraint for the attitude is only to stay inside the mandatory zone so both trajectories are really close to the fastest (and feasible) way to get to the desired attitude and will only differ slightly due to handcrafting the constants used in the algorithm.

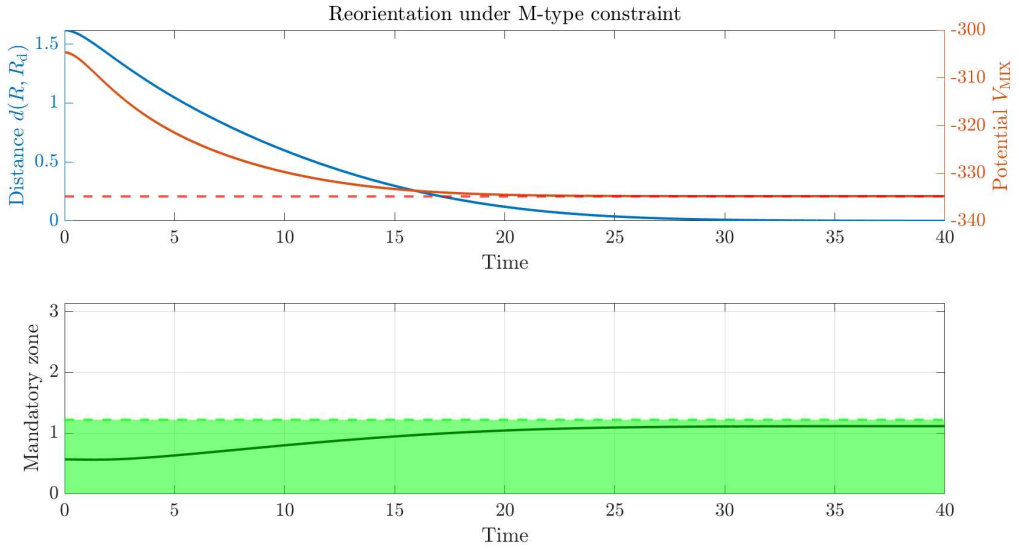

Figure 12: Numerical results obtained for the *Experiment 1.1*. Top panel: values of the distance between the actual attitude and the desired attitude, and value of the potential during reorientation; the dashed line represents the theoretically-evaluated minimum value of the potential pertaining to this experiment. Bottom panel: Angle between the boresight direction of the antenna and the mandatory direction; the green area represents the mandatory zone. Time is measured in seconds.

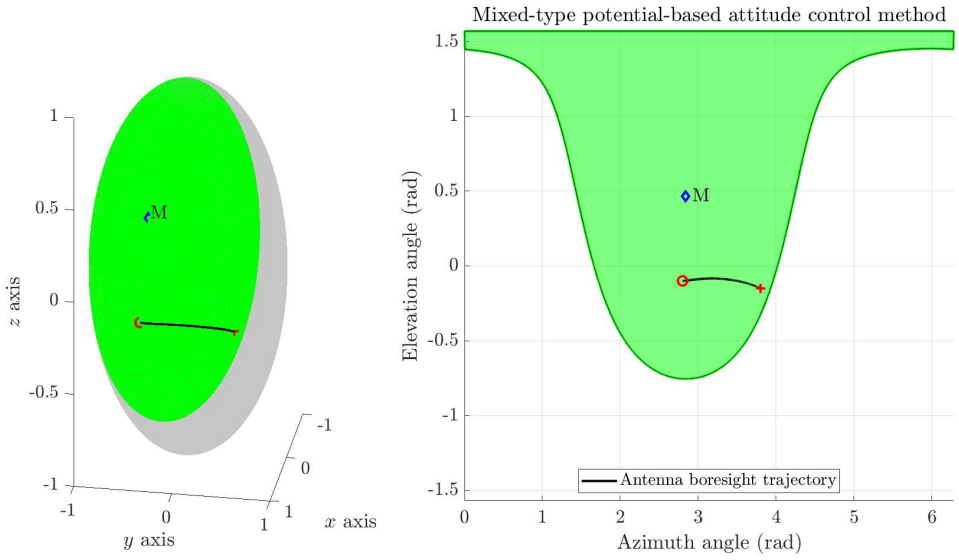

Figure 13: Trajectory achieved by the mandatory axis as explained in *Experiment 1.1*. Left panel: The trajectory is shown on a sphere that surrounds the satellite and is centered in the center of gravity of the spacecraft. Right panel: Two dimensional representation of the sphere, the mandatory zone and the trajectory of the mandatory axis. The red cross represents the attitude reached at the end of the simulation, while the red circle represents the initial attitude.

Experiment 2: The second experiment consisted in simulating reorientation in the presence of four forbidden zones, according to *Case 1a* discussed in the paper [24]. The problem will firstly be tackled by an additive-potential-based control algorithm as explained in Section 5.2. In this experiment, the potential and the associated torque read

$$\begin{cases} V_{\mathrm{ADD}}(R) = & -\frac{1}{2}K_{\mathrm{A}}\ell\exp\left(-\frac{d^2(R_{\mathrm{d}},R)}{\ell}\right) - K_{\mathrm{F}}\log(\cos\theta_{\mathrm{F1}} - e_{\mathrm{F1}}^{\top}R\,e_{\mathrm{BS}}) \\ & -K_{\mathrm{F}}\log(\cos\theta_{\mathrm{F2}} - e_{\mathrm{F2}}^{\top}R\,e_{\mathrm{BS}}) - K_{\mathrm{F}}\log(\cos\theta_{\mathrm{F3}} - e_{\mathrm{F3}}^{\top}R\,e_{\mathrm{BS}}) \\ & -K_{\mathrm{F}}\log(\cos\theta_{\mathrm{F4}} - e_{\mathrm{F4}}^{\top}R\,e_{\mathrm{BS}}), \\ T_{\mathrm{ADD}}(R) = & -K_{\mathrm{A}}\exp\left(-\frac{d^2(R_{\mathrm{d}},R)}{\ell}\right)\mathrm{Log}(R_{\mathrm{d}}^{\top}R) + \frac{K_{\mathrm{F}}}{e_{\mathrm{F1}}^{\top}R\,e_{\mathrm{BS}}-\cos\theta_{\mathrm{F1}}}\sigma(R^{\top}e_{\mathrm{F1}}e_{\mathrm{BS}}^{\top}) \\ & +\frac{K_{\mathrm{F}}}{e_{\mathrm{F2}}^{\top}R\,e_{\mathrm{BS}}-\cos\theta_{\mathrm{F2}}}\sigma(R^{\top}e_{\mathrm{F2}}e_{\mathrm{BS}}^{\top}) + \frac{K_{\mathrm{F}}}{e_{\mathrm{F3}}^{\top}R\,e_{\mathrm{BS}}-\cos\theta_{\mathrm{F3}}}\sigma(R^{\top}e_{\mathrm{F3}}e_{\mathrm{BS}}^{\top}) \\ & +\frac{K_{\mathrm{F}}}{e_{\mathrm{F4}}^{\top}R\,e_{\mathrm{BS}}-\cos\theta_{\mathrm{F4}}}\sigma(R^{\top}e_{\mathrm{F4}}e_{\mathrm{BS}}^{\top}). \end{cases} \tag{60}$$

Table 4 shows the data pertaining to this simulation tackled with a virtual additive potential. Notice that, as in the previous experiment, some constants are parameterized to the inertial coefficient J_{C} for convenience.

The numerical results obtained with an additive potential are illustrated in the Figure 14. The result achieved by the control algorithm in the given time frame is RPI = 95.8%. As it may be readily appreciated from the figure, the optimization-based control algorithm effectively attains the minimum value of the potential function while keeping the boresight of the sensor away from the forbidden cones. While the objective of avoiding forbidden areas is accomplished the desired rotation matrix is not achieved. In fact from Figure 15 can be seen that initially e_{BS} moves towards its goal, signaled by the red cross, but when the boresight approaches the directional obstacle the algorithm operates a change of trajectory to avoid entering the red area and starts coasting with a reasonable distance the forbidden space. Eventually the algorithms struggles to reach the exact orientation as it only swings by the desired attitude. From the top panel of Figure 14 it can be seen how the geodetic distance almost reaches zero around 55 seconds in the simulation but then slowly increases and never reaches its goal. Moreover, it can be seen in the bottom left panel how the boresight of the antenna once it gets close to the forbidden area number 3 starts coasting near it while maintaining distance. The combination of the behaviors just explained clarifies why the goal is not reached as two opposites constraints need to be respected , namely, reaching the goal and maintaining distance from the forbidden area. While it is true that through some manual adjustments of the constants implied in the simulation a better RPI can be reached, the problem remains because the trajectory obtained always coasts the forbidden area and then misses the objective.

Description	**Numerical value**
Initial attitude R_{i}	$\begin{bmatrix} 0.4726 & -0.3499 & -0.8089 \\ -0.8129 & 0.1814 & -0.5534 \\ 0.3404 & 0.9191 & -0.1987 \end{bmatrix}$
Desired attitude R_{d}	$\begin{bmatrix} -0.4112 & 0.4083 & 0.8150 \\ 0.8165 & 0.5625 & 0.1302 \\ -0.4053 & 0.7190 & -0.5646 \end{bmatrix}$
Forbidden direction $e_{\mathrm{F}1}$	$[-0.174\ 0.934\ -0.34]^\top$
Forbidden direction $e_{\mathrm{F}2}$	$[0\ -0.7071\ 0.7071]^\top$
Forbidden direction $e_{\mathrm{F}3}$	$[0.8532\ -0.4361\ -0.2861]^\top$
Forbidden direction $e_{\mathrm{F}4}$	$[-0.1220\ -0.1400\ -0.9830]^\top$
Aperture of the first forbidden cone $\theta_{\mathrm{F}1}$	40 (°)
Aperture of the second forbidden cone $\theta_{\mathrm{F}2}$	40 (°)
Aperture of the third forbidden cone $\theta_{\mathrm{F}3}$	30 (°)
Aperture of the fourth forbidden cone $\theta_{\mathrm{F}4}$	20 (°)
Constant K_{A}	$5 \cdot 10^{-1} J_{\mathrm{C}}$
Constant ℓ	50
Constant K_{f}	$1.5 J_{\mathrm{C}}$
Constant K_{F}	$3.5 \cdot 10^{-2} J_{\mathrm{C}}$

Table 4: Numerical data corresponding to the numerical *Experiment 2* tackled with a virtual additive potential.

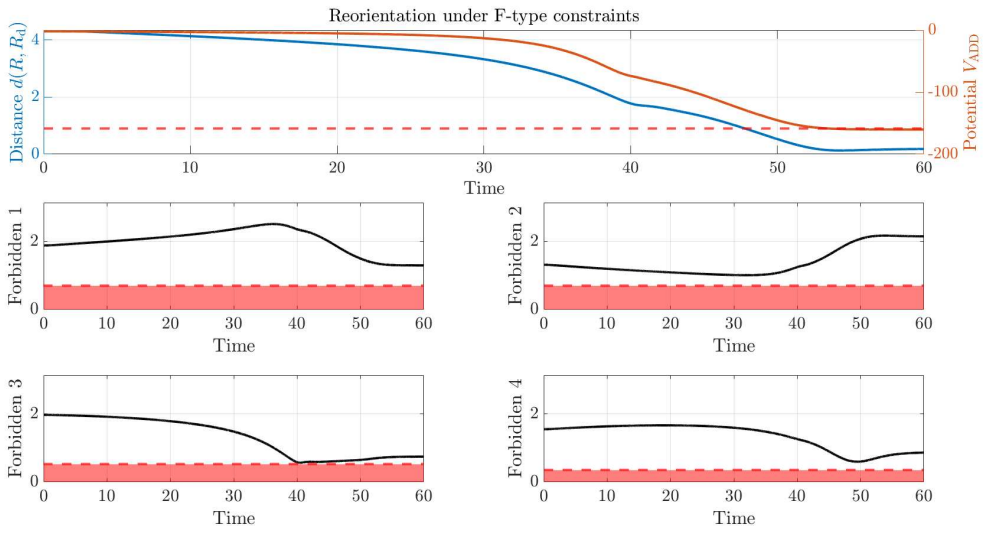

Figure 14: Numerical results obtained for the *Experiment 2*. Top panel: values of the distance between the actual attitude and the desired attitude, and value of the potential during reorientation; the dashed line represents the theoretically-evaluated minimum value of the potential pertaining to this experiment. Bottom-left and bottom-right panels: Angle between the boresight direction of the sensor and each forbidden direction; the red areas represent the forbidden zones. Time is measured in seconds.

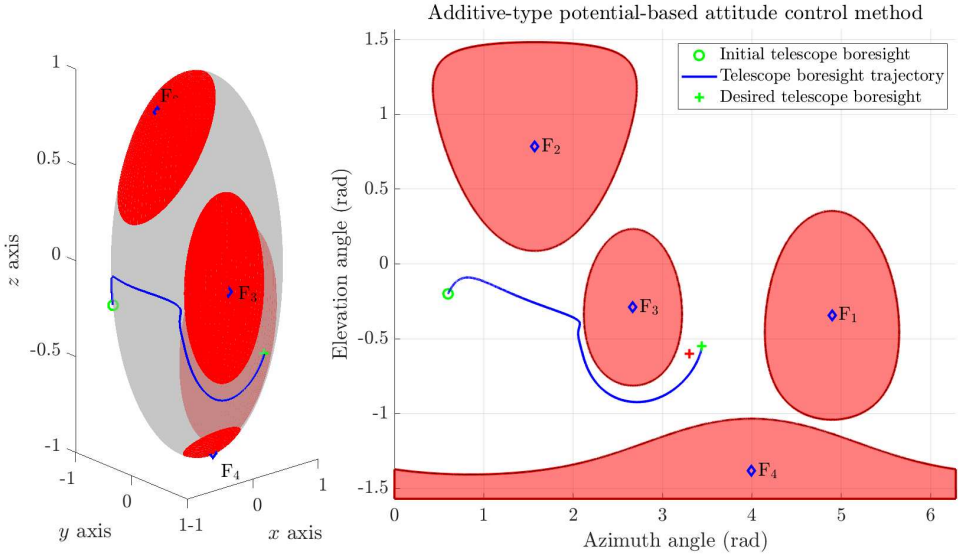

Figure 15: Numerical results obtained for the *Experiment 2*. Left panel: 3D visualization of boresight trajectory. Right panel: 2D representation of the maneuver. The green cross represents the attitude reached at the end of the simulation, while the green circle represents the initial attitude. The red cross represents the desired attitude.

Experiment 2.1: it is now proposed tackling the problem using the mixed-potential explained in Section 5.3 using the same data for initial and desired rotational matrices and also for directional obstacles and amplitudes as *Experiment 2* (6.1)while the variables used for this version of the experiment had to be handcrafted and modified to obtain a good looking trajectory: $K_{\mathrm{A}} = 2 \cdot 10^{-1} J_{\mathrm{C}}$, $\ell = 50$, $K_{\mathrm{f}} = 2 J_{\mathrm{C}}$, $K_{\mathrm{F}} = 2.8 \cdot 10^{-2} J_{\mathrm{C}}$. The torque and the potential for this case read:

$$
\begin{cases}
V_{\mathrm{MIX}}(R) = & -\frac{1}{2} K_{\mathrm{A}} \ell \exp\left(-\frac{d^2(R\mathrm{d},R)}{\ell}\right) - K_{\mathrm{F}} \frac{d^2(R_{\mathrm{d}},R)}{2} (\log(\cos\theta_{\mathrm{F1}} - e_{\mathrm{F1}}^{\top} R\, e_{\mathrm{BS}}) \\
& + \log(\cos\theta_{\mathrm{F2}} - e_{\mathrm{F2}}^{\top} R\, e_{\mathrm{BS}}) + \log(\cos\theta_{\mathrm{F3}} - e_{\mathrm{F3}}^{\top} R\, e_{\mathrm{BS}}) + \log(\cos\theta_{\mathrm{F4}} - e_{\mathrm{F4}}^{\top} R\, e_{\mathrm{BS}})), \\
T_{\mathrm{MIX}}(R) = & K_{\mathrm{A}} \exp\left(-\frac{d^2(R_{\mathrm{d}},R)}{\ell}\right) \mathrm{Log}(R_{\mathrm{d}}^{\top} R) + K_{\mathrm{F}} \log(\cos\theta_{\mathrm{F1}} - e_{\mathrm{F1}}^{\top} R\, e_{\mathrm{BS}}) \\
& + K_{\mathrm{F}} \log(\cos\theta_{\mathrm{F2}} - e_{\mathrm{F2}}^{\top} R\, e_{\mathrm{BS}}) + K_{\mathrm{F}} \log(\cos(\theta_{\mathrm{F3}} - {e_{\mathrm{F3}}}^{\top} R\, e_{\mathrm{BS}}) \\
& + K_{\mathrm{F}} \log(\cos\theta_{\mathrm{F4}} - e_{\mathrm{F4}}^{\top} R\, e_{\mathrm{BS}}) \mathrm{Log}(R_{\mathrm{d}}^{\top} R) \\
& + \frac{d^2(R_{\mathrm{d}},R)}{2} \left(\frac{K_{\mathrm{F}}}{e_{\mathrm{F1}}^{\top} R\, e_{\mathrm{BS}} - \cos\theta_{\mathrm{F1}}} \sigma(R^{\top} e_{\mathrm{F1}} e_{\mathrm{BS}}^{\top}) + \frac{K_{\mathrm{F}}}{e_{\mathrm{F2}}^{\top} R\, e_{\mathrm{BS}} - \cos\theta_{\mathrm{F2}}} \sigma(R^{\top} e_{\mathrm{F2}} e_{\mathrm{BS}}^{\top}) \right. \\
& \left. + \frac{K_{\mathrm{F}}}{e_{\mathrm{F3}}^{\top} R\, e_{\mathrm{BS}} - \cos\theta_{\mathrm{F3}}} \sigma(R^{\top} e_{\mathrm{F3}} e_{\mathrm{BS}}^{\top}) + \frac{K_{\mathrm{F}}}{e_{\mathrm{F4}}^{\top} R\, e_{\mathrm{BS}} - \cos\theta_{\mathrm{F4}}} \sigma(R^{\top} e_{\mathrm{F4}} e_{\mathrm{BS}}^{\top}) \right).
\end{cases}
\tag{61}
$$

The result obtained in Experiment 2.1 are displayed in Figure 16 and also the trajectory obtained is presented in Figure 17. Let *Trajectory 1* be the trajectory accomplished using the additive potential-based control shown in Figure 15 and *Trajectory 2* the one accomplished using the mixed potential-based control shown in Figure 17. Let's compare the trajectories obtained: firstly, it is important to notice that the desired attitude is reached only using the mixed potential-based control, in fact in Figure 17 the red cross marking the desired attitude is not visible since it coincides with the reached attitude signaled with a green cross that indicates the attitude achieved. Taking in consideration the first part of the two trajectories it is visible that while *Trajectory 1* has a more direct approach to the obstacle (*Forbidden zone number 3*), instead *Trajectory 2* moves towards the obstacle with a direction that has more slope. Let's now compare the section where the two trajectories coast around the obstacle, both have similar behaviors given that the distance slowly increases towards the end of the simulation, but even if they have a similar behavior the results differ because in the coasting phase in *Trajectory 1* is longer than *Trajectory 2* resulting in a greater distance from the obstacle and, consequently, from the goal.

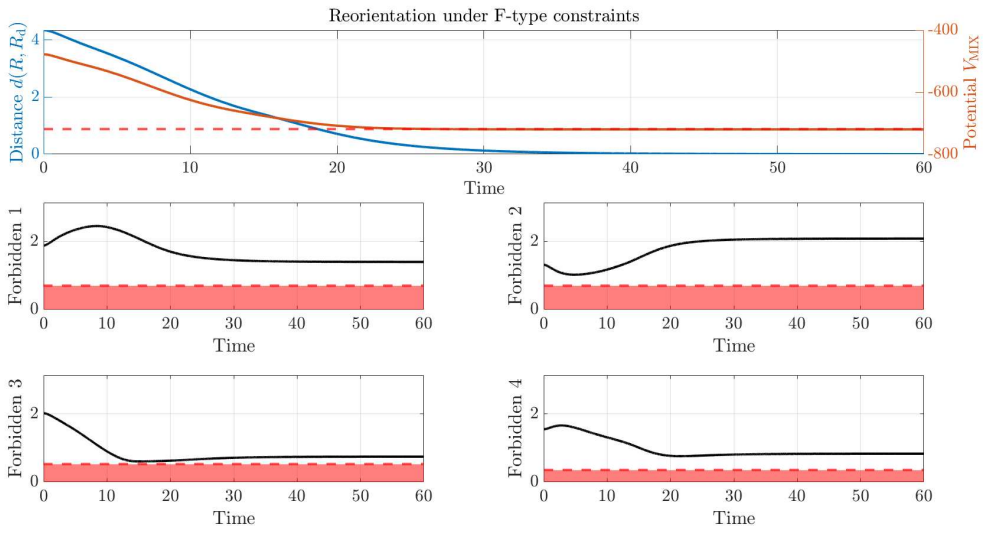

Figure 16: Numerical results obtained for the *Experiment 2.1*. Top panel: values of the distance between the actual attitude and the desired attitude, and value of the potential during reorientation; the dashed line represents the theoretically-evaluated minimum value of the potential pertaining to this experiment. Bottom-left and bottom-right panels: Angle between the boresight direction of the sensor and each forbidden direction; the red areas represent the forbidden zones. Time is measured in seconds.

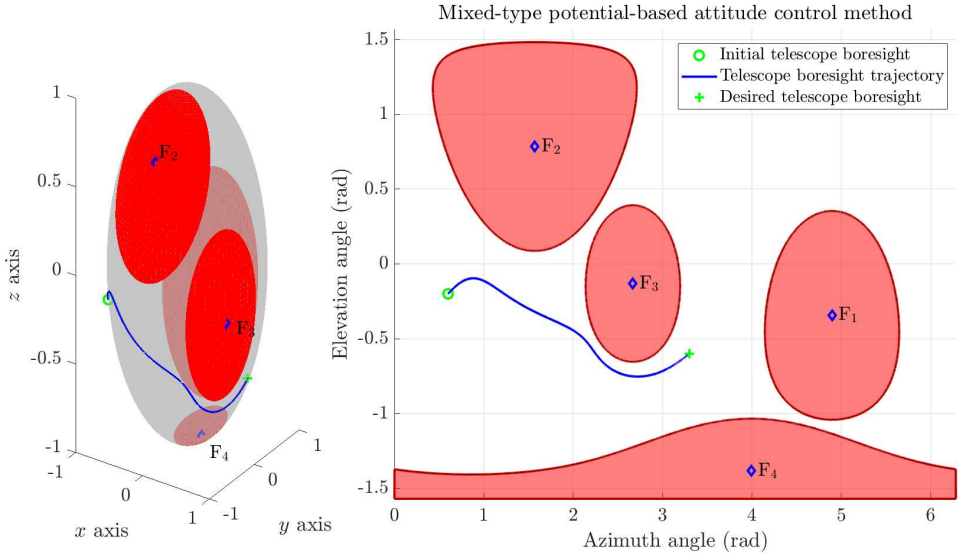

Figure 17: Numerical results obtained for *Experiment 2.1*. Left panel: 3D visualization of boresight trajectory. Right panel: 2D representation of the maneuver. The green cross represents the attitude reached at the end of the simulation and the desired one, while the green circle represents the initial attitude.

Experiment 3: the third experiment concerning reorientation is similar to *Experiment 2* with slight differences in obstacle positions and corresponds to *Case 1b* discussed in the paper [24]. Table 5 displays the values of the constants used in this simulation. In this case the potential and the associated torque are exactly the ones used in *Experiment 2* and are written in equation 60.

Description	**Numerical value**
Initial attitude R_{i}	$\begin{bmatrix} 0.4566 & 0.8892 & 0.0269 \\ 0.3579 & -0.1559 & -0.9207 \\ -0.8145 & 0.4300 & -0.3894 \end{bmatrix}$
Desired attitude R_{d}	$\begin{bmatrix} -0.8140 & 0.1648 & 0.5570 \\ 0.4620 & -0.3975 & 0.7928 \\ 0.3520 & 0.9027 & 0.2474 \end{bmatrix}$
Forbidden direction e_{F1}	$[-0.163 \ -0.986 \ 0.02]^\top$
Forbidden direction e_{F2}	$[0 \ -0.573 \ 0.819]^\top$
Forbidden direction e_{F3}	$[0.067 \ 0.462 \ -0.88]^\top$
Forbidden direction e_{F4}	$[0.813 \ -0.548 \ -0.19]^\top$
Aperture of the first forbidden cone θ_{F1}	40 (°)
Aperture of the second forbidden cone θ_{F2}	40 (°)
Aperture of the third forbidden cone θ_{F3}	20 (°)
Aperture of the fourth forbidden cone θ_{F4}	20 (°)
Initial angular speed	0_3

Table 5: Numerical data corresponding to the numerical *Experiment 3*.

As a first attempt, the problem was tackled by an additive-potential-based control algorithm as explained in Section 5.2. The values of the coefficients chosen in this experiment were $K_{\mathrm{A}} = 4.5 \cdot 10^{-1} J_{\mathrm{C}}$, $\ell = 50$, $K_{\mathrm{f}} = 3J_{\mathrm{C}}$, $K_{\mathrm{F}} = 0.1 \cdot 10^{-3} J_{\mathrm{C}}$.

The numerical results obtained with an additive potential are illustrated in the Figure 18 and the trajectory achieved is shown in Figure 19. The optimization-based control algorithm effectively attains the minimum value of the potential function while keeping the boresight of the sensor away from the forbidden cones moreover the result achieved by the control algorithm in the given time frame is RPI = 100%.

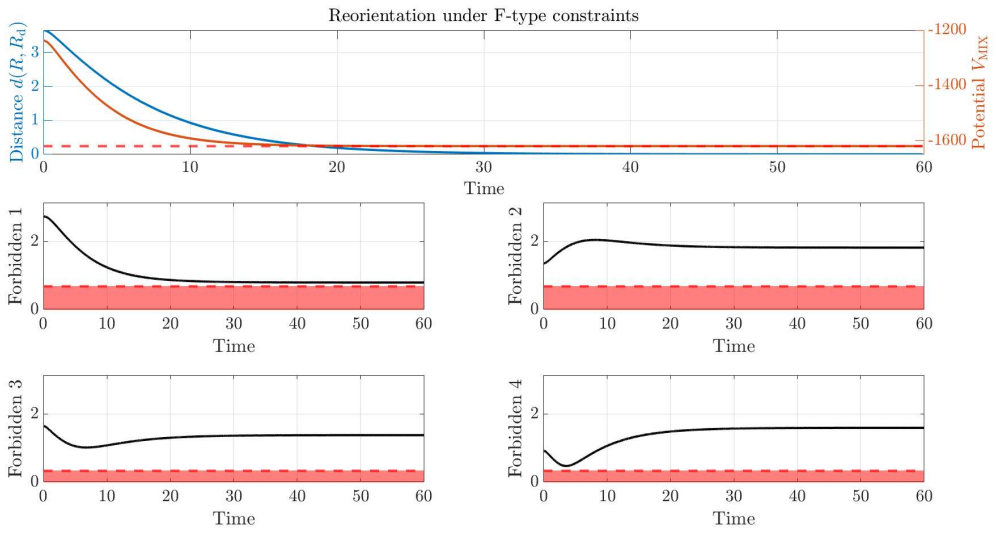

Figure 18: Numerical results obtained for the *Experiment 3* tackled with a virtual additive potential. Top-left panel: values of the distance between the actual attitude and the desired attitude, and value of the potential during reorientation; the dashed line represents the theoretically-evaluated minimum value of the potential pertaining to this experiment. Bottom-left and bottom-right panels: Angle between the boresight direction of the sensor and each forbidden direction; the red areas represent the forbidden zones. Time is measured in seconds.

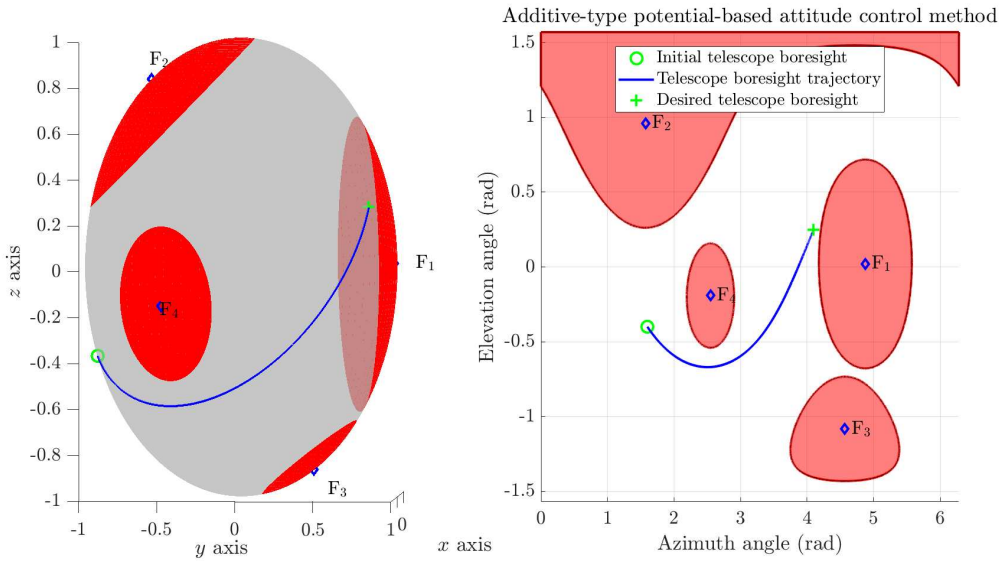

Figure 19: Numerical results obtained for the *Experiment 3*. Left panel: 3D visualization of boresight trajectory. Right panel: 2D representation of the maneuver. The green cross represents the attitude reached at the end of the simulation and the desired one, while the green circle represents the initial attitude.

Experiment 3.1: As a further attempt, the problem was tackled by a mixed additive-multiplicative potential-based approach as explained in Section 5.3. This experiment uses the potential and the associated torque that can be found in 6.1.

The values of the coefficients chosen in this experiment were $K_{\mathrm{A}} = 2.7 \cdot 10^{-1} J_{\mathrm{C}}$ $K_{\mathrm{f}} = 2J_{\mathrm{C}}$, $K_{\mathrm{F}} = 1 \cdot 10^{-3} J_{\mathrm{C}}$.

The numerical results obtained with a mixed potential are illustrated in the Figure 20 while the trajectory completed is presented in Figure 21. In this experiment, the result achieved by the control algorithm in the given time frame is RPI = 100%. In this case using two different potential-based controls has not shown any particular convenience supplying almost the exact trajectories and data.

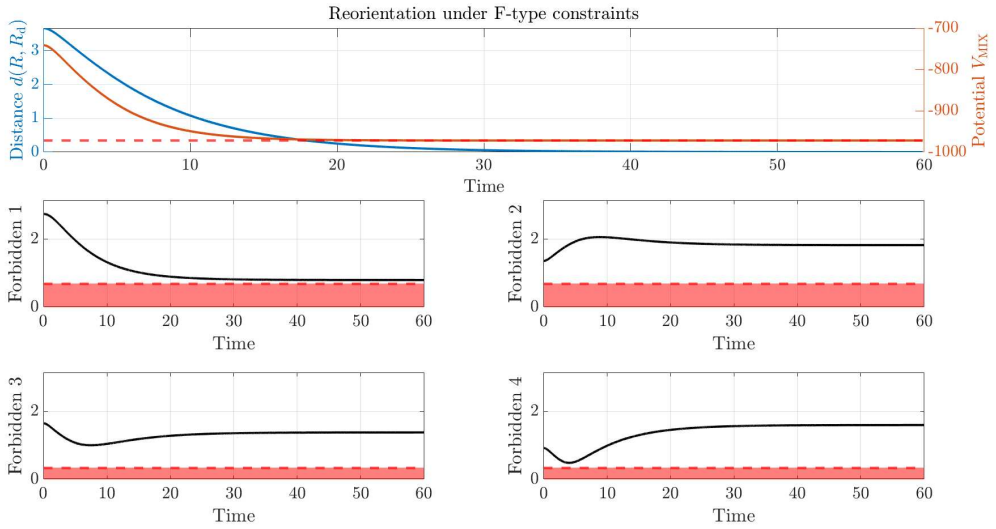

Figure 20: Numerical results obtained for the *Experiment 3.1* tackled with a virtual additive-multiplicative potential. Top-left panel: values of the distance between the actual attitude and the desired attitude, and value of the potential during reorientation. Bottom-left and right-hand panels: Angle between the boresight direction of the sensor and each forbidden direction; the red areas represent forbidden zones. Time is measured in seconds.

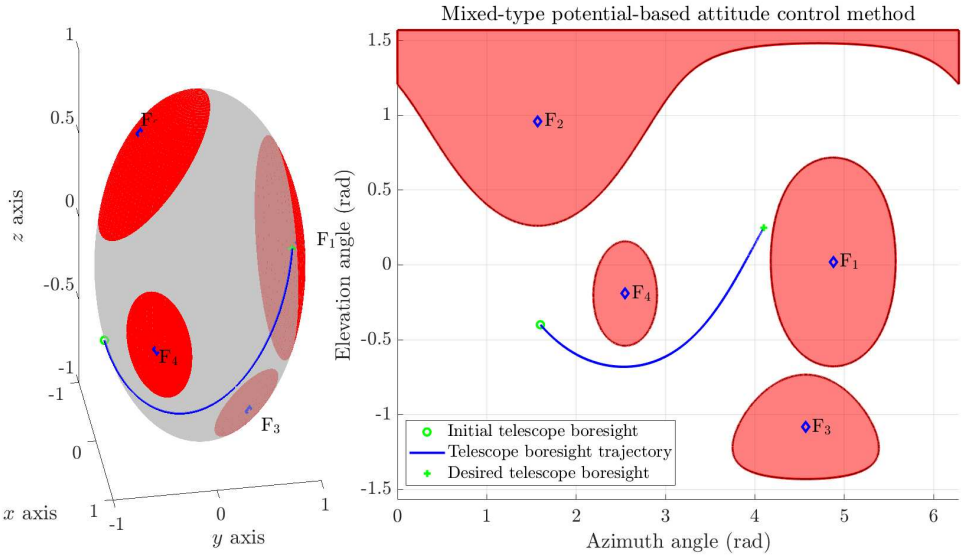

Figure 21: Numerical results obtained for the *Experiment 3.1*. Left panel: 3D visualization of boresight trajectory. Right panel: 2D representation of the maneuver. The green cross represents the attitude reached at the end of the simulation and the desired one, while the green circle represents the initial attitude.

Experiment 4: the fourth experiment concerning reorientation is based on a mandatory zone and three forbidden zones and corresponds to *Case 3* discussed in the paper [24]. Table 6 shows the reorientation data pertaining to this simulation, firstly completed using an additive potential-based control algorithm using the following equations:

$$\begin{cases} V_{\mathrm{ADD}}(R) = & -\frac{1}{2}K_{\mathrm{A}}\ell\exp\left(-\frac{d^2(R_{\mathrm{d}},R)}{\ell}\right) - K_{\mathrm{F}}\log(\cos\theta_{\mathrm{F1}} - e_{\mathrm{F1}}^{\top}R\,e_{\mathrm{BS}}) \\ & -K_{\mathrm{F}}\log(\cos\theta_{\mathrm{F2}} - e_{\mathrm{F2}}^{\top}R\,e_{\mathrm{BS}}) - K_{\mathrm{F}}\log(\cos\theta_{\mathrm{F3}} - e_{\mathrm{F3}}^{\top}R\,e_{\mathrm{BS}}) \\ & -K_{\mathrm{M}}\log(e_{\mathrm{M}}^{\top}R\,e_{\mathrm{BA}} - \cos\theta_{\mathrm{M}}), \\ T_{\mathrm{ADD}}(R) = & -K_{\mathrm{A}}\exp\left(-\frac{d^2(R_{\mathrm{d}},R)}{\ell}\right)\mathrm{Log}(R_{\mathrm{d}}^{\top}R) + \frac{K_{\mathrm{F}}}{e_{\mathrm{F1}}^{\top}R\,e_{\mathrm{BS}}-\cos\theta_{\mathrm{F1}}}\sigma(R^{\top}e_{\mathrm{F1}}e_{\mathrm{BS}}^{\top}) \\ & +\frac{K_{\mathrm{F}}}{e_{\mathrm{F2}}^{\top}R\,e_{\mathrm{BS}}-\cos\theta_{\mathrm{F2}}}\sigma(R^{\top}e_{\mathrm{F2}}e_{\mathrm{BS}}^{\top}) + \frac{K_{\mathrm{F}}}{e_{\mathrm{F3}}^{\top}R\,e_{\mathrm{BS}}-\cos\theta_{\mathrm{F3}}}\sigma(R^{\top}e_{\mathrm{F3}}e_{\mathrm{BS}}^{\top}) \\ & +\frac{K_{\mathrm{M}}}{e_{\mathrm{M}}^{\top}R\,e_{\mathrm{BA}}-\cos\theta_{\mathrm{M}}}\sigma(R^{\top}e_{\mathrm{M}}e_{\mathrm{BA}}^{\top}). \end{cases} \tag{62}$$

Description	**Numerical value**
Initial attitude R_{i}	$(0.714, 0.637, 0.13, -0.26)$
Desired attitude R_{d}	$(-0.23, -0.08, -0.491, 0.84)$
Mandatory direction e_{M}	$[0.813\ \ -0.548\ \ -0.192]^{\top}$
Forbidden direction e_{F1}	$[0\ 1\ 0]^{\top}$
Forbidden direction e_{F2}	$[0\ \ -0.819\ 0.573]^{\top}$
Forbidden direction e_{F3}	$[0.122\ 0.139\ \ -0.982]^{\top}$
Aperture of the mandatory cone θ_{M}	70 (°)
Aperture of the first forbidden cone θ_{F1}	40 (°)
Aperture of the second forbidden cone θ_{F2}	40 (°)
Aperture of the third forbidden cone θ_{F3}	20 (°)
Initial angular speed	0_3

Table 6: Numerical data corresponding to the numerical *Experiment 4*. The rotation matrix are expressed in JPL quaternion notation for the sake of notation conciseness.

The values of the coefficients chosen in this experiment were $K_{\mathrm{A}} = 4.5 \cdot 10^{-2} J_{\mathrm{C}}$, $\ell = 50$, $K_{\mathrm{f}} = 1.8 J_{\mathrm{C}}$, $K_{\mathrm{M}} = 4 \cdot 10^{-3} J_{\mathrm{C}}$, $K_{\mathrm{F}} = 6 \cdot 10^{-3} J_{\mathrm{C}}$. The results obtained with an additive potential are illustrated in the Figure 22 while in Figure 23 is displayed the trajectory of the evolution of the attitude projected in a 2 dimensions.

While the optimization-based control algorithm effectively keeps the boresight of the sensor away from the forbidden cones and the boresight of the antenna within the mandatory zone, the attained orientation does not match at all the desired one and also the algorithm is not able to reach the minimum of the potential function. In fact the result achieved by the control algorithm in the given time frame is only RPI = 32.3%.

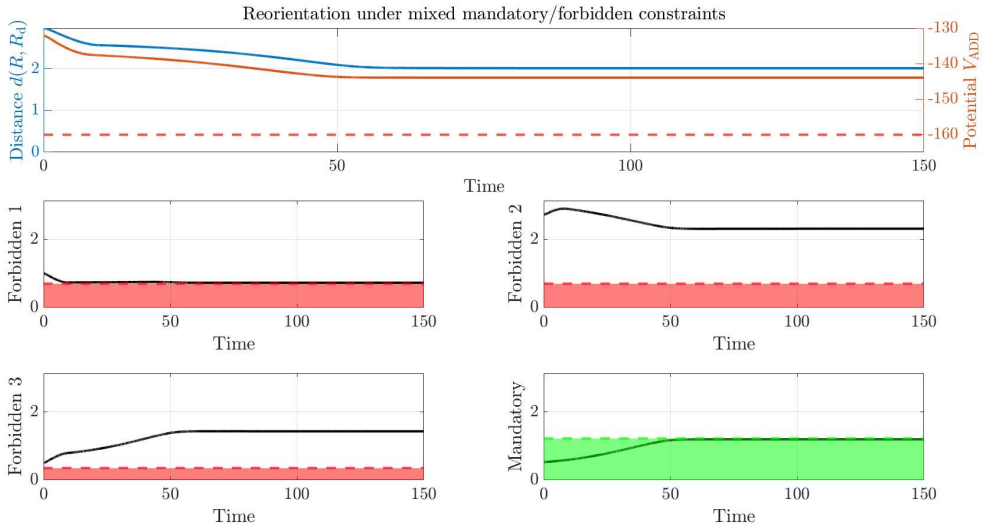

Figure 22: Numerical results obtained for the *Experiment 4* tackled with a virtual additive potential. Top-left panel: values of the distance between the actual attitude and the desired attitude, and value of the potential during reorientation; the dashed line represents the theoretically-evaluated minimum value of the potential pertaining to this experiment. Time is measured in seconds. Notice the behavior of panel "***Forbidden 1***" and "***Mandatory***", this is explained in 6.1 in *Experiment 4.1*.

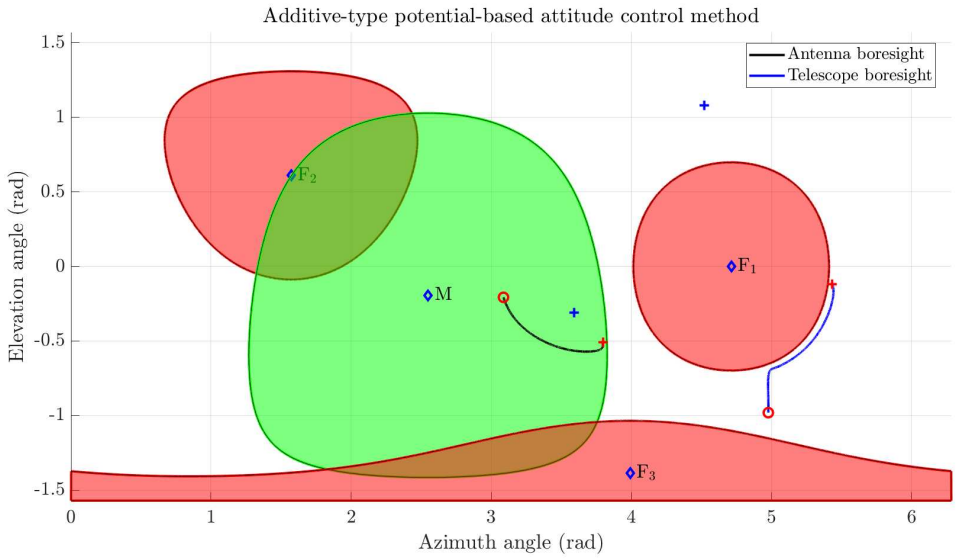

Figure 23: Trajectory obtained for *Experiment 4* tackled with a virtual additive potential. The red crosses represent the attitude reached at the end of the simulation, the blue crosses represent the desired attitude and finally the red circles represent the initial attitude.

Experiment 4.1: As a further attempt, the problem was tackled by a mixed additive-multiplicative potential-based approach as explained in Section 5.3. The values of the coefficients chosen in this experiment were $K_{\mathrm{f}} = 2.5 J_{\mathrm{C}}$, $K_{\mathrm{M}} = 1.5 \cdot 10^{-1} J_{\mathrm{C}}$, $K_{\mathrm{F}} = 1.2 \cdot 10^{-2} J_{\mathrm{C}}$. The numerical results obtained with a mixed potential are illustrated in the Figure 24 and the trajectory is displayed in Figure 25 while the potential and torque related to this experiment read:

$$
\begin{cases}
V_{\mathrm{MIX}}(R) = & -\frac{1}{2} K_{\mathrm{A}} \, \ell \exp\left(-\frac{d^2(R\mathrm{d},R)}{\ell}\right) - \frac{1}{2} d^2(R\mathrm{d},R) \, (K_{\mathrm{M}} \log(e_{\mathrm{M}}^{\top} R \, e_{\mathrm{BA}} - \cos\theta_{\mathrm{M}}) \\
& + K_{\mathrm{F}} \log(\cos\theta_{\mathrm{F1}} - e_{\mathrm{F1}}^{\top} R \, e_{\mathrm{BS}}) + K_{\mathrm{F}} \log(\cos\theta_{\mathrm{F2}} - e_{\mathrm{F2}}^{\top} R \, e_{\mathrm{BS}}) \\
& + K_{\mathrm{F}} \log(\cos\theta_{\mathrm{F3}} - e_{\mathrm{F3}}^{\top} R \, e_{\mathrm{BS}}) + K_{\mathrm{F}} \log(\cos\theta_{\mathrm{F4}} - e_{\mathrm{F4}}^{\top} R \, e_{\mathrm{BS}})), \\
T_{\mathrm{MIX}}(R) = & -K_{\mathrm{A}} \exp\left(-\frac{d^2(R_{\mathrm{d}},R)}{\ell}\right) \mathrm{Log}(R_{\mathrm{d}}^{\top} R) + K_{\mathrm{F}} \log(\cos\theta_{\mathrm{F1}} - e_{\mathrm{F1}}^{\top} R \, e_{\mathrm{BS}}) \\
& + K_{\mathrm{F}} \log(\cos\theta_{\mathrm{F2}} - e_{\mathrm{F2}}^{\top} R \, e_{\mathrm{BS}}) + K_{\mathrm{F}} \log(\cos\theta_{\mathrm{F3}} - {e_{\mathrm{F3}}}^{\top} R \, e_{\mathrm{BS}}) \\
& + K_{\mathrm{F}} \log(\cos\theta_{\mathrm{F4}} - e_{\mathrm{F4}}^{\top} R \, e_{\mathrm{BS}}) \mathrm{Log}(R_{\mathrm{d}}^{\top} R) \\
& + \frac{d^2(R_{\mathrm{d}},R)}{2} \left(\frac{K_{\mathrm{F}}}{e_{\mathrm{F1}}^{\top} R \, e_{\mathrm{BS}} - \cos\theta_{\mathrm{F1}}} \sigma(R^{\top} e_{\mathrm{F1}} e_{\mathrm{BS}}^{\top}) + \frac{K_{\mathrm{F}}}{e_{\mathrm{F2}}^{\top} R \, e_{\mathrm{BS}} - \cos\theta_{\mathrm{F2}}} \sigma(R^{\top} e_{\mathrm{F2}} e_{\mathrm{BS}}^{\top}) \right. \\
& \left. + \frac{K_{\mathrm{F}}}{e_{\mathrm{F3}}^{\top} R \, e_{\mathrm{BS}} - \cos\theta_{\mathrm{F3}}} \sigma(R^{\top} e_{\mathrm{F3}} e_{\mathrm{BS}}^{\top}) + \frac{K_{\mathrm{F}}}{e_{\mathrm{F4}}^{\top} R \, e_{\mathrm{BS}} - \cos\theta_{\mathrm{F4}}} \sigma(R^{\top} e_{\mathrm{F4}} e_{\mathrm{BS}}^{\top}) \right).
\end{cases}
\tag{63}
$$

The result achieved by the control algorithm in the given time frame is RPI = 100%. Comparing the results obtained in *Experiment 4* and *Experiment 4.1* the difference is substantial, in fact first of all the trajectories follow two completely different paths and end up with very different RPI percentages. In *Experiment 4* the path chosen by the algorithm makes the boresight of the telescope go towards the right of the forbidden zone number one as seen in Figure 23 while instead in *Experiment 4.1* the telescope boresight goes towards the left of the obstacle. By going to the right of the obstacle, in Figure 23 we can see that the trajectory in the given time frame stops (before reaching the desired attitude signaled with blue crosses) in such way that the telescope boresight is very close to the forbidden zone number 1 while the antenna boresight is very close to the barrier of the mandatory zone, this is due to physical constraints. In fact the trajectory encounters a point in which the satellite physically cannot go beyond because the angle between the right most outer part of the forbidden zone and the mandatory zone create an angle that is greater than the angle between the boresight of the antenna and the telescope. If the algorithm decides to iterate (keep moving in that direction) further more than the points marked with two red crosses in 23 (one in the mandatory zone and one near forbidden zone 1) one constraints of the two would be broken and either the antenna would exit the mandatory zone or the telescope would fall inside of the obstacle.

To better understand the situation, refer to Figure 22 . Notice that, in the bottom panels of the picture, two particular behaviors out of the four depicted just skim the surface of respectively, the green and red area, denoting that the directional constraints are dangerously close to be broken.

In *Experiment 4.1* instead the algorithm runs a different approach making the telescope boresight pass through the left side of obstacle 1 which results in avoiding the singular situation just explained. In fact first thing first the antenna boresight moves away from the desired attitude and once the telescope has avoided the obstacle both boresights of the antenna and the telescope can finally move towards the desired attitude (two red crosses this time overlap the two blue crosses seen in Figure 23 because the attitude reached coincides with the desired one) finally satisfying both constraints given.

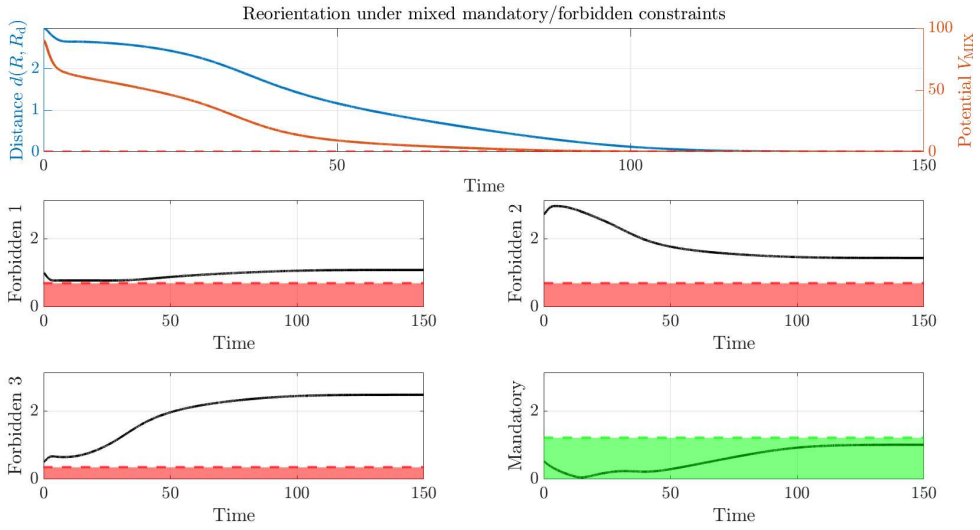

Figure 24: Numerical results obtained for the *Experiment 4.1* tackled with a virtual additive-multiplicative potential. Top-left panel: values of the distance between the actual attitude and the desired attitude, and value of the potential during reorientation. Bottom-left and bottom-right panels: Angle between the boresight direction of the sensor and each forbidden direction, as well as angle between the boresight direction of the antenna and the mandatory direction; the red areas represent forbidden zones while the green area represent the mandatory zone. Time is measured in seconds.

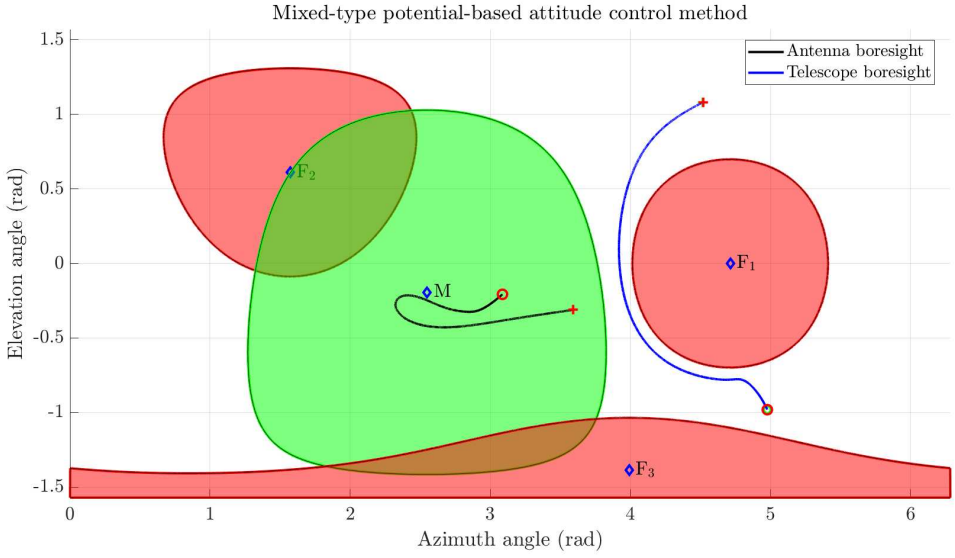

Figure 25: Trajectory obtained for the *Experiment 4.1* tackled with a virtual additive-multiplicative potential. The two red circles at the start of antenna and telescope trajectory represent their start points, while the red crosses represent the final and desired points of the two.

6.2 Numerical simulations about rendezvous

A number of experiments concerning rendezvous has been completed. A first set of experiments was performed in the presence of obstacles whose position is fixed with respect to the reference frame $\mathcal{F}_{\mathrm{S}}$. The second set of experiments was devoted to testing the behavior of the guidance algorithm in the presence of moving obstacles. The third set of experiments was, instead, dedicated to evaluating the performance of a guidance strategy that consists in joint translation and attitude control.

Experiment 1. The first experiment was performed by assuming the presence of obstacles whose position is fixed with respect to the reference frame $\mathcal{F}_{\mathrm{S}}$. The aim of this experiment is to compare the performances of the three control strategies described in Section 5.5 in terms of propellant consumption. In this experiment is set $h = 0.01$ (sec).

The initial location, desired location and initial speed are summarized in Table 7.

Description	**Value**
Initial location p_{i}	$[-16{,}100\ 0\ 3{,}000]^{\top}$ (m)
Initial speed $\dot{p}_{\mathrm{i}}$	$[-0.5\ 0\ 0.01]^{\top}$ (m/s)
Desired location p_{d}	$[0\ 0\ 150]^{\top}$ (m)

Table 7: Reference values for the *Experiment 1* about cruising phase. We recall that the Z (or R_{bar}) axis points toward the Earth, hence a quota of 150 m in the LVLH reference frame indicates a target location below the station (as seen from the Earth).

It's important to point out that the control algorithm is implemented in such a way that the cruising phase is deemed concluded whenever the distance between the spacecraft and the target is less than 50 m. Table 8 shows the location of four obstacles along with their safety radius.

Safety radius (m)	**Location (m)**
$\eta_1 = 650$ (m)	$o_1 = [-10{,}000\ 0\ 1{,}500]^{\top}$ (m)
$\eta_2 = 350$ (m)	$o_2 = [-5{,}500\ 0\ 1900]^{\top}$ (m)
$\eta_3 = 150$ (m)	$o_3 = [-2{,}800\ 0\ 0]^{\top}$ (m)
$\eta_4 = 50$ (m)	$o_4 = [-2{,}100\ 0\ 200]^{\top}$ (m)

Table 8: Location and safety radius of the obstacles ordered by size. All obstacles happen to locate below the station (as seen from the Earth).

In this experiment the components of random disturbance F_{rd} are zero-mean random Gaussian variables with standard deviation of 100 N. Notice that the random disturbance takes a non-zero component along the y axis, henceforth, if the motion of the spacecraft will take place slightly off the $x-z$ plane the control algorithm will need to compensate for such unwanted effect (the desired position is located on the vertical plane, in fact).

The numerical results are illustrated in Figure 26, which shows the trajectory of the spacecraft along the $x-z$ plane in the LVLH coordinate frame, and in Figure 27, which shows the trajectory of the spacecraft along the landscape of the virtual potential function used to achieve automated guidance.

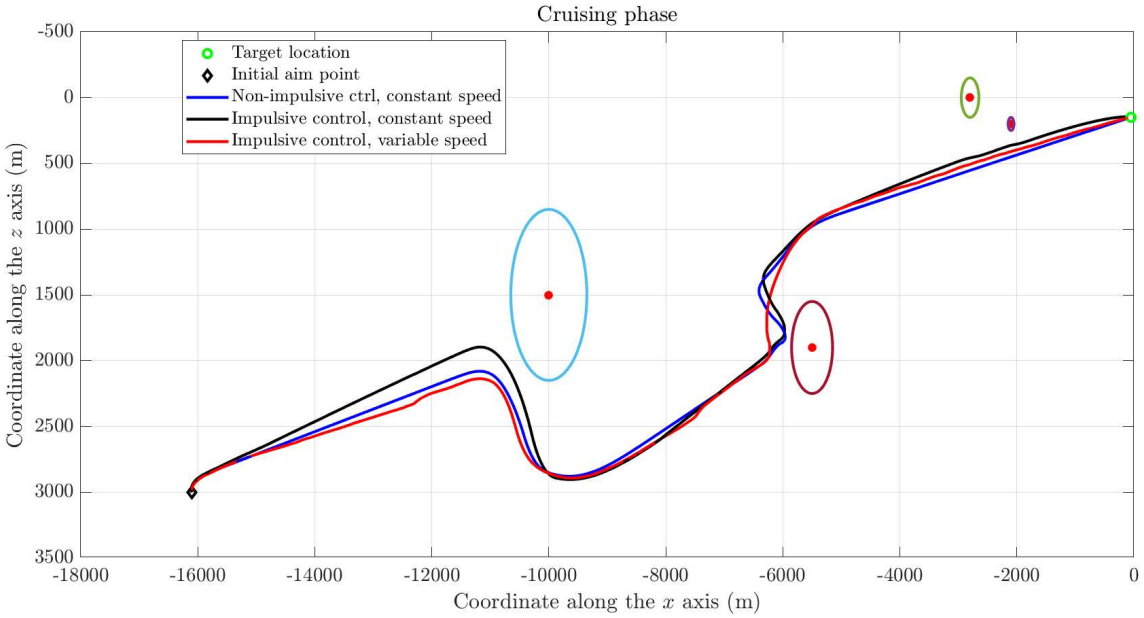

Figure 26: Numerical results obtained for the *Experiment 1* about cruising phase: Trajectory in the LVLH coordinate frame. Recall that the X (or V_{bar}) axis points toward the direction of motion over the orbit, hence a negative value of the x coordinate indicates a spacecraft that is, in fact, chasing the space station from behind. The ovals denote the boundaries of the safety regions surrounding each obstacle.

In particular, Figure 26 shows how the spacecraft is enabled to traverse the space, keeping sufficiently far from the obstacles while approaching the target location. The results displayed in this figure show that, in the absence of obstacles, the spacecraft is driven to take the shortest route, except for the case where, in the vicinity of the obstacles, the spacecraft is forced to turn around the safety surface of the obstacles found on its path, hence taking a detour from a straight path. The degree of curvature depends certainly on the chosen values of the parameters, which may be subject to a more or less conservative design, and on the safety radii of the obstacles which, to some extent, depend on the sensitivity range of the sensors mounted aboard the spacecraft. Notice that it was assumed that the space station has mapping abilities and provides a detailed map of the main obstacles sites and sizes so that a spacecraft endowed with proximity sensors may safely navigate through them.

On the other hand, Figure 27 serves to illustrate the shape and the function of the devised potential energy function. The landscape of the potential presents a global minimum corresponding to the desired location as well as four peaks in correspondence to the obstacles central location. The trajectory of the spacecraft develops bypassing the areas of higher potential while "rolling down" toward the minimal-potential location.

Such results were obtained by setting the values of the parameters defined in the context of attractive-repulsive potential as $H_{\text{A}} = 10^{-2}$ and $H_{\text{R}} = 10^{6}$. The obtained trajectories appear quite similar to one another and the three control strategies are able to achieve the desired location where the cruising phase ends.

However, the consumption of propellant resulting from the application of the three control strategies results to be quite different. The consumption resulting from the three regulation strategies are displayed in the Figure 28.

The introduction of impulsive control hence results in a sensible reduction of propellant consumption compared to non-impulsive regulation. Furthermore, the reduction of total mass corresponding to the regulation algorithm based on impulsive control with variable desired speed versus the one with constant-speed case are similar, depending on various cases it produces a better or worse performance. This happens because of a different behavior at the end of cruising phase. While the former control, thanks to its lowest speed at the end of the cruising phase, follows the desired direction and so takes a shorter route to the far-end phase end point, the latter control

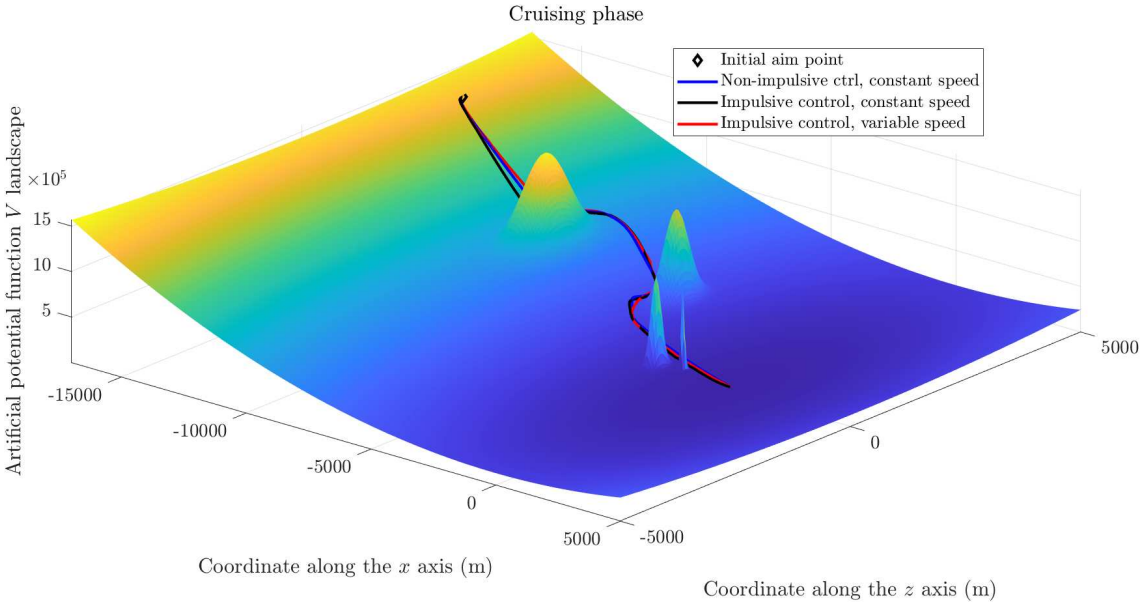

Figure 27: Numerical results obtained for the *Experiment 1* about cruising phase: Trajectory along the landscape of the virtual potential function.

(constant speed) is less affected by changes of trajectory due to an higher speed because, again, compared to the variable-speed approach, this method "does not sense" to be about to reach the target and keeps the same speed (maximum feasible for this phase) while the method with variable speed decreases velocity as it gets closer to the goal. This explains why the red line in Figure 28 decreases later in time with respect to the black one and in a more gradual manner achieving also slightly lower fuel consumption.

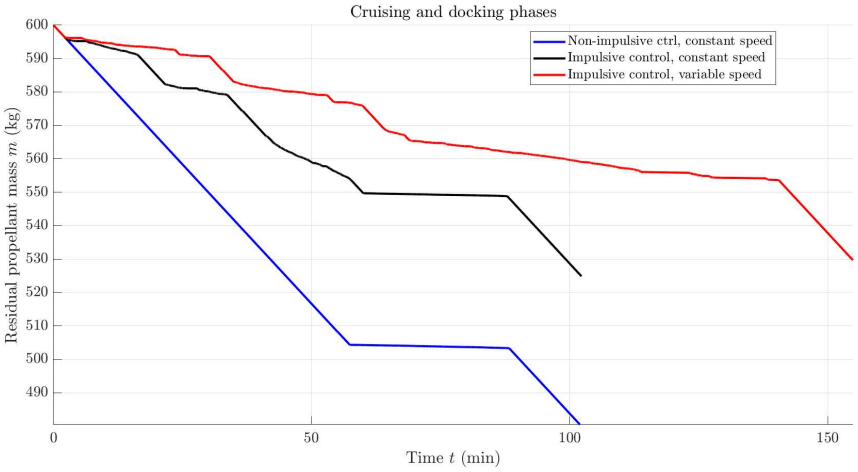

Figure 28: Numerical results obtained for the *Experiment 1* about cruising phase: Cold gas consumption.

A further element of evaluation of the control strategies under comparison is the final speed upon reaching the predefined target location. No control requirements were defined on this matter, hence the control strategies do not embody any information about a final desired speed. However, the regulation strategy based on variable speed implicitly makes the final speed vanish to zero since it is proportional to the distance to the target. The effects of explicit speed limitation is illustrated in Figure 29, from which it is apparent how, in this instance, the spacecraft arrives ready to start the docking sequence while the other two types of control first need a broader trajectory to lower their speed.

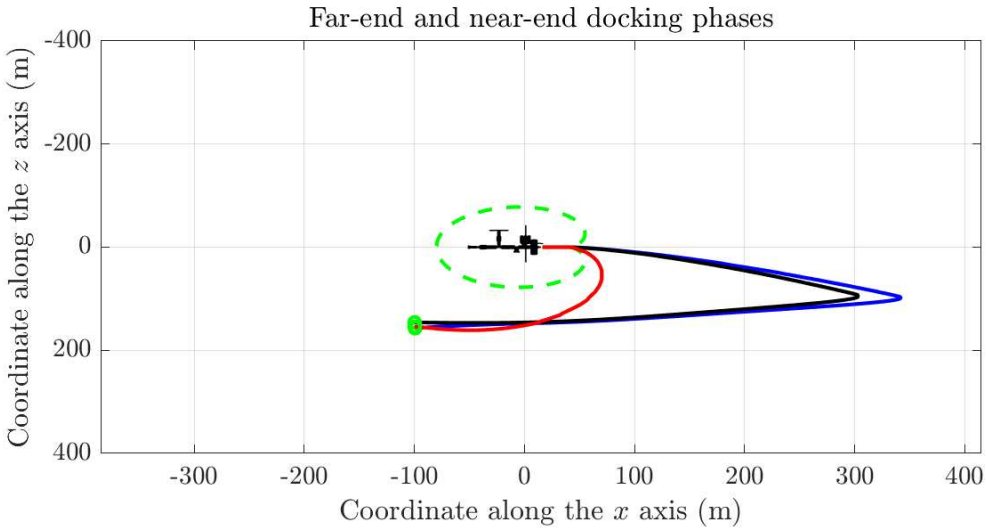

Figure 29: Numerical results obtained for the *Experiment 1* about cruising phase: Detail of the final guidance maneuver to attain docking. The color code is the same as in previous figures concerning *Experiment 1*. $H_{\mathrm{t}} = 1$ for all the docking phase.

The position at which the far-end maneuver stops is indicated as $p_{\mathrm{fe}} \in \mathbb{R}^3 = [40\ 0\ 0]^\top$ (m), while the position at which the near-end maneuver stops is indicated as $p_{\mathrm{ne}} \in \mathbb{R}^3 = [15\ 0\ 0]^\top$ (m). Notice that the final target p_{ne} is located 15 m right to the center of the station – whose coordinate in the $\mathcal{F}_{\mathrm{S}}$ system is $[0\ 0\ 0]^\top$ by definition – to comply with the actual position of the docking port.

Because of the above-mentioned evaluation elements, it has been deemed appropriate to perform the following experiments only on the basis of the impulsive-control with variable-speed regulation strategy.

Since in the experiments a disturbance is present even along the y axis, it is interesting to evaluate the effects of such disturbance on the ability of a spacecraft to adhere to the orbital plane. The control strategies do not have as explicit goal to keep the motion of a spacecraft over the vertical $(x-z)$ plane but the final guidance implicitly attains such goal. The Figure 30 shows the effects of the disturbances on the y coordinate of the spacecraft in the LVLH reference frame. Is worthily to highlight how in the proximity of the first obstacle along the route, corresponds a peak of off-orbit displacement, this result is a consequence of the repulsive force, which is important due to the radius of that obstacle, combined with natural y displacement caused by random disturbances.

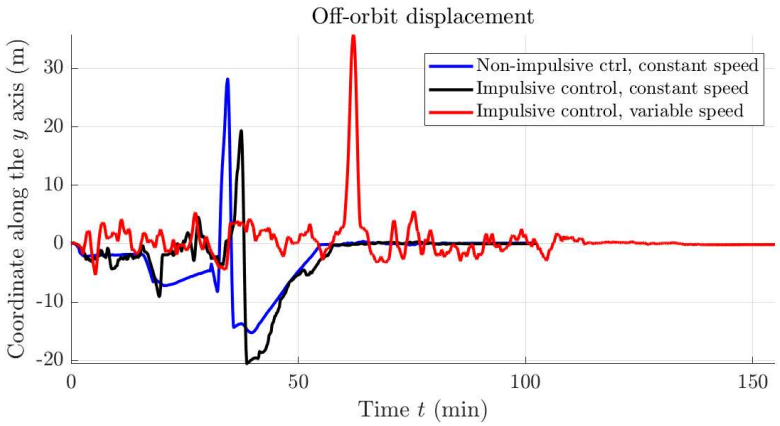

Figure 30: Numerical results obtained for the *Experiment 1* about cruising phase: Detail of the off-orbit effect caused by random disturbances.

Experiment 2. The aim of the second experiment is to verify the correct behavior of the guidance algorithm of the first experiment in a case of moving obstacles. We considered the same obstacles as *Experiment 1*, considering though that their position is now changing over time in a uniform rectilinear motion by setting an initial speed and a direction angle. Every obstacle is considered moving on the x-z plane in the LVLH coordinate frame. The initial conditions are shown in Table 9.

Figure 31 shows the trajectory of the spacecraft during the cruising phase. As shown in the figure, the algorithm behave correctly near the obstacles by directing the spacecraft away from obstacles' motion direction (dashed circles represent position and safety radii of obstacles), while it performs as usual for the last two fixed obstacles.

As already described, to ensure the avoidance we considered a spacecraft provided with sensors capable to detects debris and other obstacles from enough distance or a spacecraft already provided with the position of each obstacles over time.

No other major differences can be evaluated between this experiment and the previous one because the results about propellant consumption and off-orbit displacement depends majorly from the obstacles direction and speed.

Speed (m/s)	**Direction angle (°)**
$\nu_1 = 1$ (m/s)	$\theta_1 = 140$ (°)
$\nu_2 = 0.5$ (m/s)	$\theta_2 = -80$ (°)
$\nu_3 = 0$ (m)	$\theta_3 = 0$ (°)
$\nu_4 = 0$ (m)	$\theta_4 = 0$ (°)

Table 9: Speed and direction angles of the obstacles ordered by size. Note that the last two obstacles are not moving.

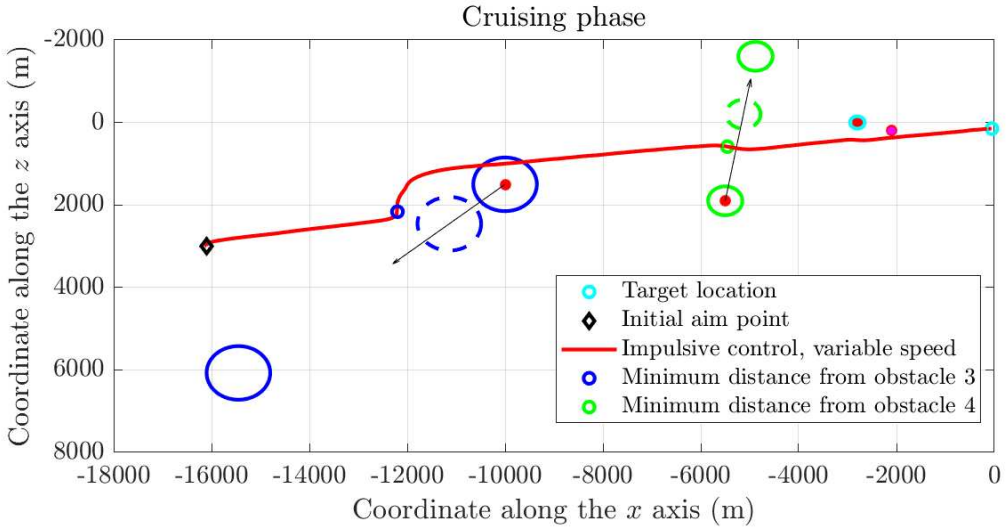

Figure 31: Numerical results obtained for the *Experiment 2* about cruising phase: Obstacles moving in a uniform rectilinear motion. The blue and green dashed lines represent the position, respectively, of obstacle 3 and obstacle 4, at minimum distance from spacecraft during cruising phase. While the continuous blue and green ovals without a red dot inside are the final positions of moving obstacles.

Experiment 3. The purpose of the third experiment on rendezvous operation was to evaluate how the merging of position and orientation controls affect the performance of spacecraft guidance algorithm.

In the present experiment, random disturbances on the mechanical torque affecting the orientation of the spacecraft were taken into account. In particular, the non-entries of the term T_{rd} were chosen to be zero-mean Gaussian random variables of standard deviation 0.01 N·m.

Four attitude-regulation control torques were tested, corresponding to the cases discussed in Section 5.8. The values of the parameters were chosen to be $K_{\mathrm{S}} = 2.5\, J_{\mathrm{C}}$, $K_{\mathrm{FBP}} = 0.002\, J_{\mathrm{C}}$ and $K_{\mathrm{f}} = 2.5\, J_{\mathrm{C}}$. (As in the previous experiments, the coefficients are parameterized as units or fractions of the inertia coefficients J_{C} for convenience.) The numerical results are illustrated in Figure 32, which shows the trajectory of the spacecraft along the $x - z$ plane in the LVLH coordinate frame.

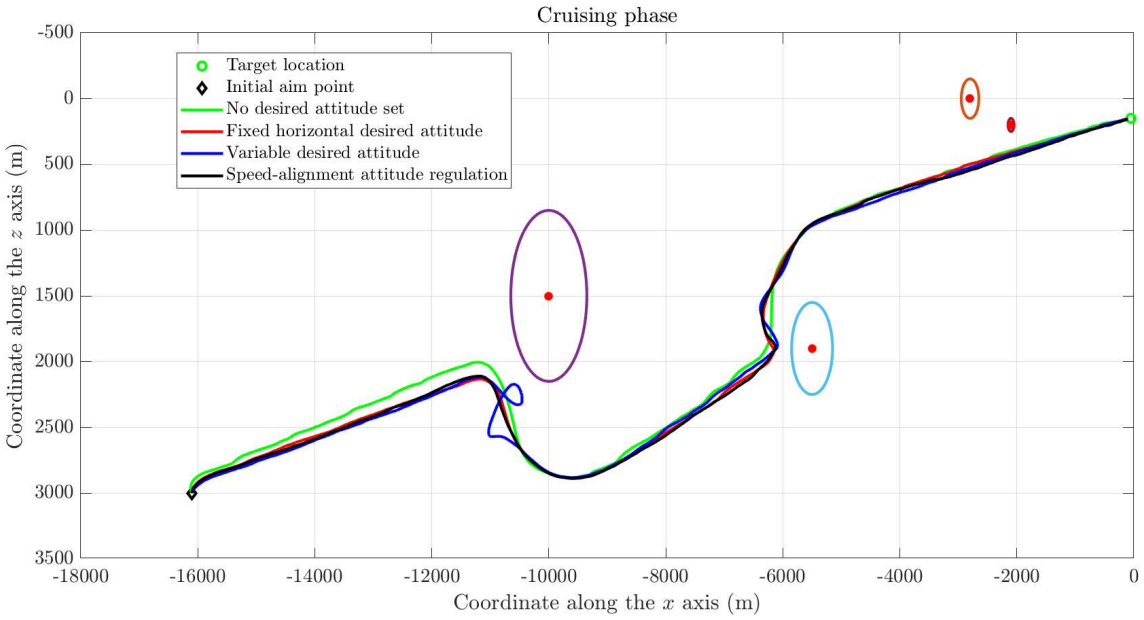

Figure 32: Numerical results obtained for the *Experiment 3* about cruising phase: Trajectory in the LVLH coordinate frame.

From this figure it appears clearly that the variable-desired-attitude strategy fails in the proximity of the largest obstacle. On the other hand, the strategy based on not setting a desired attitude, the one based on a fixed (horizontal) attitude and the ones based on velocity alignment perform similarly to one another.

The above results tell that the best performing control strategy corresponds to setting a constant desired attitude (which, in the present endeavor, was chosen to be the docking orientation). It should be, however, recognized that the strategy that entails the least consumption of propellant consists in not operating the reaction wheels at all during the cruising phase, hence leaving the spacecraft at the mercy of inertia and little accidental impacts with small debris.

During the docking maneuver, both position and orientation regulation are of prime importance, to guarantee that the spacecraft approaches the docking port of the space station at the right location and with the right orientation.

Figure 33, shows the trajectory of the spacecraft along the $x-z$ plane in the LVLH coordinate frame during docking phase. From the figure, it is readily observed that in all cases the trajectory

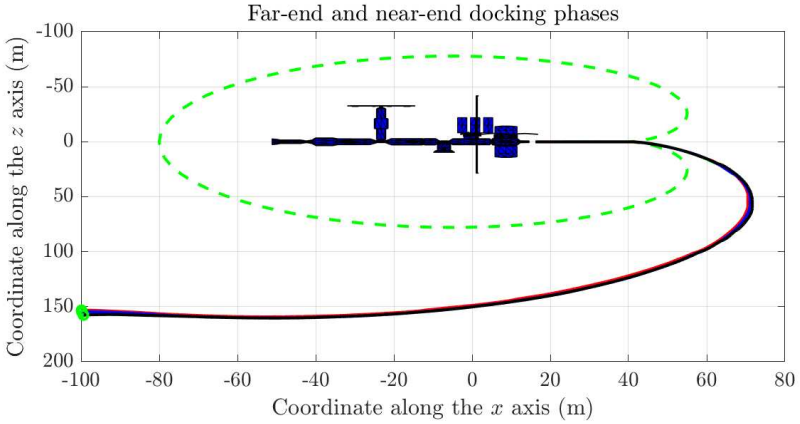

Figure 33: Numerical results obtained for the *Experiment 3* about docking phase: Trajectory in the LVLH coordinate frame. (Since the Z axis actually points toward the Earth, the picture looks upside down.) The dashed green line represent the safety cardioid-shaped contour that the spacecraft should keep out of.

of the spacecraft keeps well behind the safety contour during the far-end-approaching phase, while the near-end-approaching maneuver drives the spacecraft straight behind the docking port.

As a further element of evaluation in Figure 34 is shown the velocity of the spacecraft along the x and z axis in the LVLH coordinate frame during the whole rendezvous maneuver.

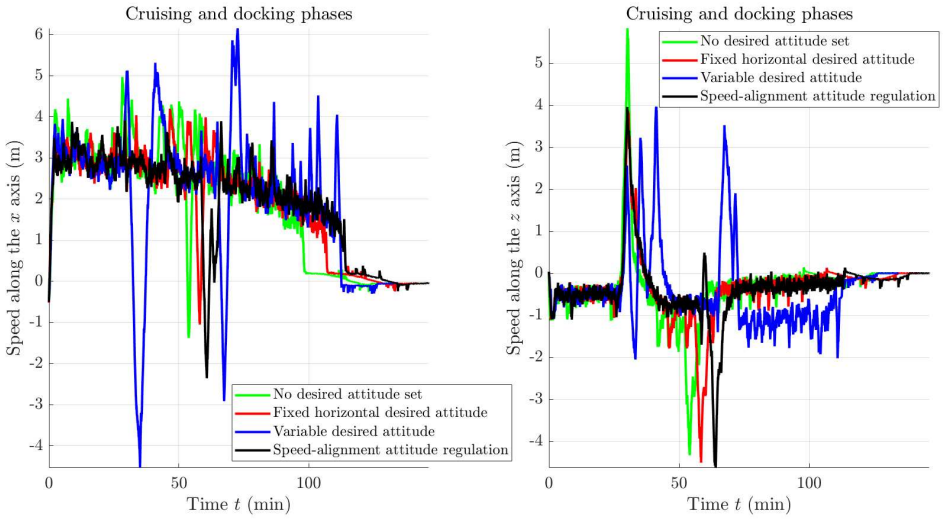

Figure 34: Numerical results obtained for the *Experiment 3* about rendezvous: Velocity of the spacecraft in the LVLH coordinate frame.

The velocity curves corresponding to a variable-speed, impulsive control strategy in connection with the four discussed orientation regulation methods show that the no-desired-attitude and the variable-desired-attitude methods stand out negatively. Such methods, as a matter of fact, causes a sudden rise of velocity in the proximity of large obstacles. Figure 35, shows the consumption of propellant during the whole rendezvous maneuver. Vertical lines within the figure stand as delimiters of the three different phases of rendezvous (cruising, far-end approach and near-end approach).

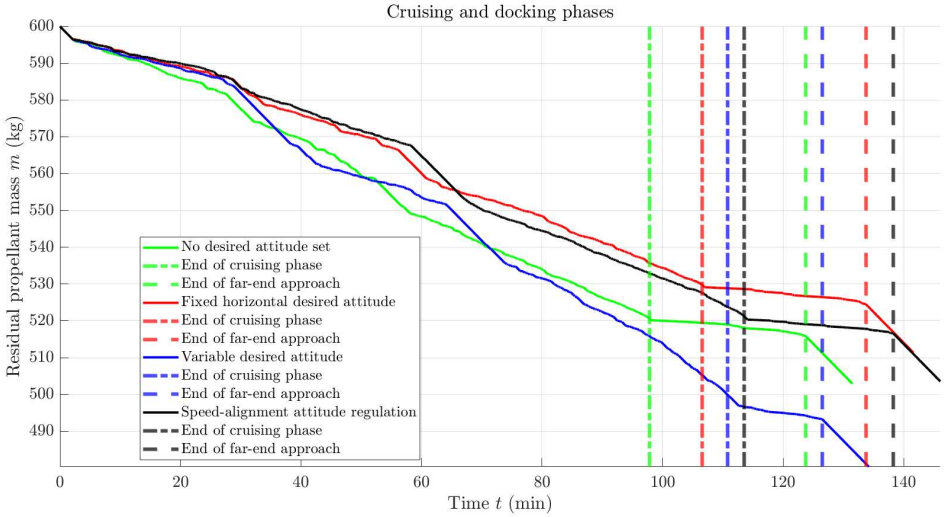

Figure 35: Numerical results obtained for the *Experiment 3* about rendezvous: Propellant consumption.

From the mass-decay curves it emerges that most propellant is consumed during the cruising phase. Also, the curves show that the fixed-horizontal-attitude strategy causes the most limited consumption of propellant during the entire rendezvous maneuver.

In addition to the above elements, to evaluate the behavior of the control strategies under examination, Figure 36 shows the orientation of the spacecraft along the entire rendezvous maneuver in terms of Euler angles computed on the basis of the instantaneous attitude matrix-indicator R.

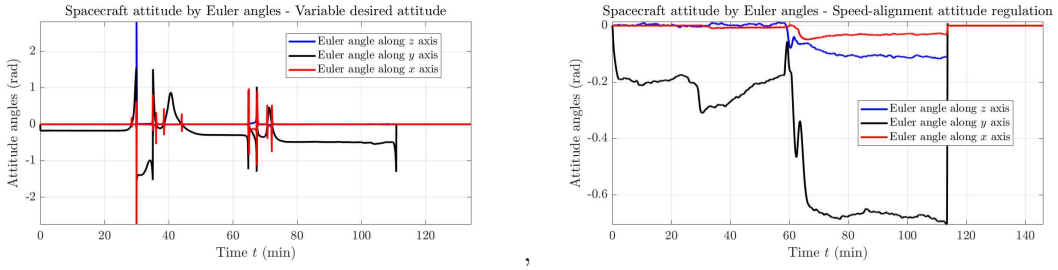

Figure 36: Numerical results obtained for the *Experiment 3* about rendezvous: Euler angles computed on the basis of the instantaneous attitude matrix-indicator R.

It is immediate to notice that the speed-alignment-based attitude control strategy does not stand as particularly appealing as it leads to a very low convergence rate and, if sped up, entails an excessive disturbance to the navigation algorithm.

It is important to remark that the choice of a constant desired attitude is possible only if the spacecraft is provided with a sufficient number of on board proximity sensor positioned all over the spacecraft, if that is not possible due to different reasons, the best choice would be to let the chaser pointing always toward the space station, but this strategy has not been elaborated in the present research.

6.3 Illustration of a complete rendezvous maneuver

From the previous evaluated experiments, a complete maneuver is performed from initial aim point to a docking port through cruising, far-end approaching and near-end approaching.

Figure 37 illustrates the cruising and docking phases. The shown result is performed using the variable-speed impulsive control algorithm explained in Section 5.7 and, for attitude control, fixed horizontal desired attitude strategy described in Section 5.8, these already mentioned strategies are the most suitable for cruising phase among the ones studied in this thesis (weaknesses and strengths are evaluated in *Experiment 1* and *Experiment 3*). The far-end and near-end phases are performed as described in Sections 5.9 and 5.10. All constants used come from *Experiment 3*.
A smooth trajectory is performed across the obstacles and around the space station, while the spacecraft keeps enough far from the radii of the obstacles and from the cardioid region. A fixed attitude control strategy is able to point the spacecraft toward the docking axis and, as seen in *Experiment 3*, to reduce the propellant consumption. Hence, the solution obtained ensures a steady rendezvous and stable trajectory during all three phases.

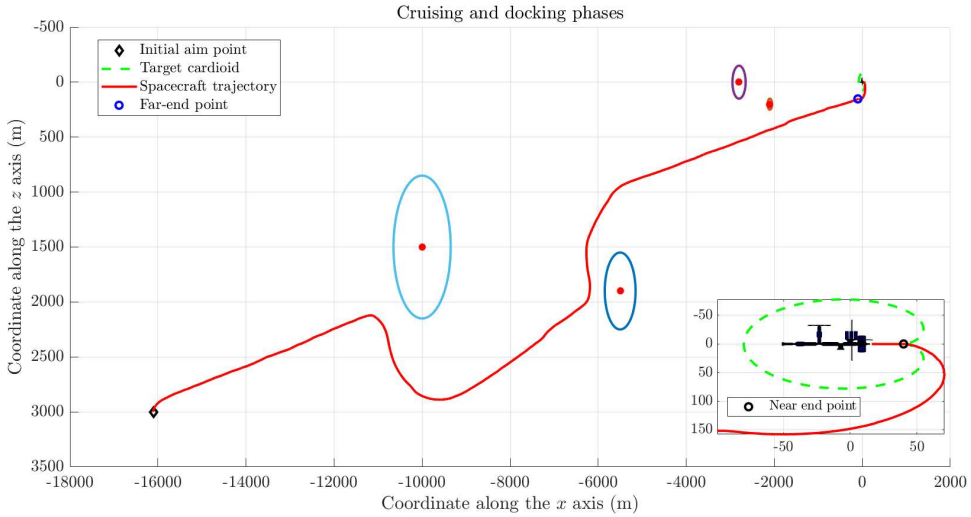

Figure 37: Complete rendezvous from initial point to docking port: Trajectory in the LVLH coordinate frame. The main plot shows the complete trajectory from the initial aim point to the arrival docking port, while the box is a zoom in of far-end and near-end approaching.

7 Conclusions

The aim of the present thesis was to propose a framework to model, simulate and control a small unmanned spacecraft, orbiting in close proximity of a space station, through manifold calculus. Two maneuvers were modeled and simulated, that is, reorientation under directional constraints and rendezvous in the presence of fixed as well as moving obstacles.

Obstacle avoidance was traditionally considered a high-level planning problem, while in recent research endeavors part of such task has been shown to be manageable by real-time low-level control algorithms [21]. The present document follows such modern line of research and is based on multi-objective optimization.

The main theoretical instrument utilized in the present research project is that of virtual attractive-repulsive potential. In fact, a physical object moves in a force field derived as anti-gradient of a potential function which embodies localized information about the spacecraft to be guided and the surrounding environment. It was believed that the complexity of tasks that can be tackled by means of this approach is limited, because of local minima in the potential function [21] which may lead a controlled object to a stable configuration different from the intended goal. However, it has been shown even by the present contribution that virtual-potential-based guidance, if properly designed and tuned, shows ability to lead to acceptable results under reasonable tolerance levels.

A distinguishing feature of the present endeavor was that, unlikely most research papers in the area that invoke the use of coordinates or quaternions, the mathematical model of the roto-translational motion of a spacecraft as well as the design of control fields were written in a coordinate-free Lie-group-type fashion.

A number of numerical experiments, aimed at complementing the theoretical developments, were discussed to illustrate the achieved progress and to guide the reader though a series of evaluations. Such evaluation stages were aimed at establishing which control strategy, among various possible combinations, appears to be the most convenient one.

During the development of the present project, a number of minor issues emerged which would need a closer examination.

An aspect to pay attention to is the effect of repulsive fields far away from the obstacles, either physical and directional, which may drive a spacecraft slightly off-track with respect to the intended target. Such problem has been dealt with by tuning the constant parameters in the guidance algorithm, although a hard-limiting strategy would perhaps prove more effective as it would cut off completely the repulsive fields whenever sufficiently far from their source.

A further aspect to pay attention to concerns alignment of a spacecraft attitude to a docking axis during final guidance in a robust way. Currently, final guidance is performed by setting up a torque term that tends to keep the reference frame $\mathcal{F}_{\mathrm{C}}$ aligned to the frame $\mathcal{F}_{\mathrm{S}}$ irrespective of possible orientation constraints or disturbances. Attitude control during such phase may be made more robust by introducing mandatory as well as forbidden directions and by enriching the torque control field by components related to such directional constraints.

8 Acknowledgments

I would like to thank Professor Simone Fiori as he supported me thoroughly during the research and gave me the chance to complete this work while being abroad in Japan, I express deep gratitude to my colleagues Francesco Rachiglia and Edoardo Sampaolesi for the time, experiences and work done together at TUAT and UNIVPM. I would like to gratefully thank Prof. Toshihisa Tanaka (Tokyo University of Agriculture and Technology – TUAT, Japan) for hosting me at the Department of Electrical and Electronic Engineering of the TUAT (Koganei campus) during March – May, 2023 in the completion of this work as I was supported by a grant from the *CampusWorld* programme of the Università Politecnica delle Marche (Italy).

This work puts and end to a chapter of my life and a beginning to a new one, I couldn't achieve what I did without the help of those who always stood beside me and supported me starting from my family: Christele, Monica and Raffaele who most of the times believed in me more than I believed in myself, who always gave me the tranquility of having someone to rely on as well as putting me in the very best conditions to achieve my goals, thank you for the unconditioned love that I will hardly ever be able to repay. Thanks to Anna Maria whom love and memories will never go lost. Thanks to Arianna for becoming such a precious and essential part of my life, for supporting me during this path by confronting and expressing myself , to be the one that always gets me and balance myself. I finally extend my gratitude to all my friends from high school, volleyball, university and to all of whom supported me in any way for which I retain myself so fortunate.

Luca Sabatini

References

[1] A. Bartoszewicz and J. Żuk, *Sliding mode control — Basic concepts and current trends*, in 2010 IEEE International Symposium on Industrial Electronics, 2010, pp. 3772–3777.

[2] J. L. Baxter, E. K. Burke, J. M. Garibaldi, and M. Norman, *Multi-robot search and rescue: A potential field based approach*, in Autonomous Robots and Agents, S. C. Mukhopadhyay and G. S. Gupta, eds., Springer Berlin Heidelberg, Berlin, Heidelberg, 2007, pp. 9–16.

[3] A. Bloch, P. Krishnaprasad, J. Marsden, and G. de Alvarez, *Stabilization of rigid body dynamics by internal and external torques*, Automatica, 28 (1992), pp. 745–756.

[4] N. Bloise, E. Capello, M. Dentis, and E. Punta, *Obstacle avoidance with potential field applied to a rendezvous maneuver*, Applied Sciences, 7 (2017).

[5] A. Bongers and J. Torres, *Orbital debris and the market for satellites*, Ecological Economics, 209 (2023).

[6] R. S. Chandrasekaran, L. J. Colombo, M. Camarinha, R. Banavar, and A. Bloch, *Variational collision and obstacle avoidance of multi-agent systems on Riemannian manifolds*, in 2020 European Control Conference (ECC), 2020, pp. 1689–1694.

[7] H. Cheng and K. C. Gupta, *An historical note on finite rotations*, Journal of Applied Mechanics, 56 (1989), pp. 139–145.

[8] W. Clohessy and R. Wiltshire, *Terminal guidance system for satellite rendezvous*, Journal of the Aerospace Sciences, 27 (1960), pp. 653–658.

[9] S. Fiori, *Model formulation over Lie groups and numerical methods to simulate the motion of gyrostats and quadrotors*, Mathematics, 7 (2019).

[10] S. Fiori, *Manifold calculus in system theory and control – Fundamentals and first-order systems*, Symmetry, 13 (2021), p. 2092.

[11] ——, *Manifold calculus in system theory and control – Second order structures and systems*, Symmetry, 14 (2022), p. 1144.

[12] S. Fiori, L. Bigelli, and F. Polenta, *Lie-group type quadcopter control design by dynamics replacement and the virtual attractive-repulsive potentials theory*, Mathematics, 10 (2022), p. 1104.

[13] S. Fiori, I. Cervigni, M. Ippoliti, and C. Menotta, *Extension of a PID control theory to Lie groups applied to synchronising satellites and drones*, IET Control Theory & Applications, 14 (2020), pp. 2628–2642.

[14] S. Fiori and L. Del Rossi, *Minimal control effort and time Lie-group synchronisation design based on proportional-derivative control*, International Journal of Control, (2022), pp. 138–150.

[15] H. Gong, W. Tang, B. Tan, and L. Wang, *Analysis of docking tolerance capability of underwater tool-switching device*, Journal of Physics: Conference Series, 1748 (2021), p. 062045.

[16] H. B. Hablani, *Attitude commands avoiding bright objects and maintaining communication with ground station*, Journal of Guidance, Control, and Dynamics, 22 (1999), pp. 759–767.

[17] Q. Hu, B. Chi, and M. R. Akella, *Anti-unwinding attitude control of spacecraft with forbidden pointing constraints*, Journal of Guidance, Control, and Dynamics, 42 (2019), pp. 822–835.

[18] L. Huang, *Velocity planning for a mobile robot to track a moving target – A potential field approach*, Robotics and Autonomous Systems, 57 (2009), pp. 55–63.

[19] I. Kamon, E. Rimon, and E. Rivlin, *TangentBug: A range-sensor-based navigation algorithm*, The International Journal of Robotics Research, 17 (1998), pp. 934–953.

[20] I. Kamon and E. Rivlin, *Sensory-based motion planning with global proofs*, IEEE Transactions on Robotics and Automation, 13 (1997), pp. 814–822.

[21] O. Khatib, *Real-time obstacle avoidance for manipulators and mobile robots*, The International Journal of Robotics Research, 5 (1986), pp. 90–98.

[22] D. Koditschek and E. Rimon, *Robot navigation functions on manifolds with boundary*, Advances in Applied Mathematics, 11 (1990), pp. 412–442.

[23] M. C. Lee and M. G. Park, *Artificial potential field based path planning for mobile robots using a virtual obstacle concept*, in Proceedings of the 2003 IEEE/ASME International Conference on Advanced Intelligent Mechatronics (AIM 2003), vol. 2, 2003, pp. 735–740.

[24] U. Lee and M. Mesbahi, *Feedback control for spacecraft reorientation under attitude constraints via convex potentials*, IEEE Transactions on Aerospace and Electronic Systems, 50 (2014), pp. 2578–2592.

[25] E. Leonard and E. Fiorelli, *Virtual leaders, artificial potentials and coordinated control of groups*, Proceedings of the 40th IEEE Conference on Decision and Control, (2001), pp. 2968–2973.

[26] H. Levine, W.-J. Rappel, and I. Cohen, *Self-organization in systems of self-propelled particles*, Physical Review E, 63 (2000).

[27] I. Lopez and C. R. McInnes, *Autonomous rendezvous using artificial potential function guidance*, Journal of Guidance, Control, and Dynamics, 18 (1995), pp. 237–241.

[28] C. R. Mclnnes, *Large angle slew maneuvers with autonomous sun vector avoidance*, Journal of Guidance, Control, and Dynamics, 17 (1994), pp. 875–877.

[29] B. Nguyen, Y.-L. Chuang, D. Tung, C. Hsieh, Z. Jin, L. Shi, D. Marthaler, A. Bertozzi, and R. Murray, *Virtual attractive-repulsive potentials for cooperative control of second order dynamic vehicles on the Caltech MVWT*, in Proceedings of the 2005 American Control Conference, (Portland, OR, USA), June 2005, pp. 1084–1089.

[30] S. Paternain, D. E. Koditschek, and A. Ribeiro, *Navigation functions for convex potentials in a space with convex obstacles*, IEEE Transactions on Automatic Control, 63 (2018), pp. 2944–2959.

[31] Y. Rasekhipour, A. Khajepour, S. Chen, and B. Litkouhi, *A potential field-based model predictive path-planning controller for autonomous road vehicles*, IEEE Transactions on Intelligent Transportation Systems, 18 (2017), pp. 1255–1267.

[32] J. Ries, R. Eanes, C. Shum, and M. Watkins, *Progress in the determination of the gravitational coefficient of the Earth*, Geophysical Research Letters, 19 (1992), pp. 529–531.

[33] E. Rimon and D. Koditschek, *Exact robot navigation using artificial potential functions*, IEEE Transactions on Robotics and Automation, 8 (1992), pp. 501–518.

[34] R. E. Roberson and R. Schwertassek, *Dynamics of multibody systems*, Springer-Verlag Berlin Heidelberg, 1988.

[35] D. Schneider, *Non-holonomic Euler-Poincaré equations and stability in Chaplygin's sphere*, Dynamical Systems, 17 (2002), pp. 87–130.

[36] S. Shimoda, Y. Kuroda, and K. Iagnemma, *Potential field navigation of high speed unmanned ground vehicles on uneven terrain*, in Proceedings of the 2005 IEEE International Conference on Robotics and Automation, 2005, pp. 2828–2833.

[37] S. Spurgeon, *Sliding mode control: a tutorial*, in 2014 European Control Conference (ECC), 2014, pp. 2272–2277.

[38] G. Sutton and O. Biblarz, *Rocket Propulsion Elements – An introduction to the engineering of rockets*, Wiley-Interscience, 7 ed., 2000.

[39] V. Utkin, *Sliding mode control design principles and applications to electric drives*, IEEE Transactions on Industrial Electronics, 40 (1993), pp. 23–36.

[40] G. Wang, Z. Xie, X. Mu, S. Li, F. Yang, H. Yue, and S. Jiang, *Docking strategy for a space station container docking device based on adaptive sensing*, IEEE Access, 7 (2019), pp. 100867–100880.

Appendix:

Unit-quaternion to rotation-matrix conversion precision

In a computer code, a unit quaternion denotes a point on a 4D hypersphere S^3 and a 3D rotation matrix denotes an element on the special orthogonal group SO(3) up to machine precision. While a rotation matrix is seldom expressed directly through its numerical entries, a quaternion often is. When the entries of a quaternion are describe by a small number of digits, e.g. by four decimal digits, its conversion to a rotation matrix does not result in a true rotation. The conversion of a quaternion $[q_i\ q_j\ q_k\ q_0]^\top$ written in JPL notation to a rotation matrix R may be expressed as

$$\tilde{R} = \begin{bmatrix} 1-2(q_j^2+q_k^2) & 2(q_iq_j-q_kq_0) & 2(q_iq_k+q_jq_0) \\ 2(q_iq_j+q_kq_0) & 1-2(q_i^2+q_k^2) & 2(q_jq_k-q_iq_0) \\ 2(q_iq_k-q_jq_0) & 2(q_jq_k+q_iq_0) & 1-2(q_i^2+q_j^2) \end{bmatrix},$$

where q_0 denotes the real part of the quaternion. To fix non-unitarity, a projection to the SO(3) group has been added based on singular value decomposition (SVD), namely

$$UDV^\top = \tilde{R},\ R := UV^\top,$$

where U, V denote the orthogonal factors of the SVD.